

# A Deep Convective Systems Database Derived from the Intercalibrated Meteorological Geostationary Satellite Fleet and the TOOCAN algorithm (2012-2020)

5 Thomas Fiolleau<sup>1</sup> and Rémy Roca<sup>1</sup>

<sup>1</sup>Université de Toulouse, LEGOS (CNRS/UT3), Toulouse France

*Correspondence to:* Thomas Fiolleau (thomas.fiolleau@cnr.fr)

## Abstract.

10 We introduce two databases aimed at facilitating the study of deep convective systems (DCS) and their morphological characteristics over the intertropical belt during the period spanning from 2012 to 2020: TOOCAN and CACATOES. The TOOCAN database is constructed using a tracking algorithm called TOOCAN applied on a homogenized GEOring infrared (IR) archive and enables the documentation of the morphological parameters of each DCS throughout its life cycle. The homogenized GEOring IR database has been built from level-1 data of a fleet of geostationary platforms originating from  
15 various sources and has been inter-calibrated, spectrally adjusted, and limb darkening corrected, specifically for the high cold cloud onto a common reference, the IR channel of the ScaRaB radiometer on-board Megha-Tropiques. The resulting infrared observations are then homogeneous for Brightness Temperatures (BT) < 240 K with a standard deviation lower than 1.5 K throughout the GEOring. A systematic uncertainty analysis is carried out. First, the radiometric errors are shown to have a little impact on the DCS characteristics and occurrences. We further evaluate the impact of missing data and demonstrate that  
20 a maximum of 3 hours of consecutive missing images represents a favorable compromise for maintaining tracking continuity while minimizing the impact on the DCS morphological parameters. However, beyond this temporal threshold, the segmentation of DCS is significantly compromised, necessitating the interruption of the tracking process. The CACATOES database is derived from the TOOCAN database through a post-processing procedure, which involves projecting the morphological parameters of each deep convective system (DCS) onto a  $1^\circ \times 1^\circ$ -1-day grid. This resultant dataset provides a  
25 broader perspective, allowing for an Eulerian analysis of the DCS and facilitating comparisons with auxiliary gridded datasets on the same daily  $1^\circ \times 1^\circ$  grid box.

Both the TOOCAN and CACATOES databases are provided on a common netCDF format that is compliant with Climate and Forecast (CF) Convention and Attribute Convention for Dataset Discovery (ACDD) standards.

A total of  $15 \times 10^6$  DCS have been identified over the tropical regions and the 9-year period. The analysis of DCS over the tropical oceans and continents reveals a large variety of DCS characteristics and organization. They can last from few hours up to several days, and their cloud shield ranges from  $1000 \text{ km}^2$  to a few millions of  $\text{km}^2$ . Oceanic DCS are characterized by a longer lifetime duration and larger shields. Finally, the DCS geographical distribution is in line with previous DCS climatology built from other algorithms and satellite observations.

All datasets can be accessed via the repository under the following data DOI:

- 35 - TOOCAN database: <https://doi.org/10.14768/1be7fd53-8b81-416e-90d5-002b36b30cf8> (Fioleau and Roca, 2023)
- CACATOES database: <https://doi.org/10.14768/98569eea-d056-412d-9f52-73ea07b9cdca> (Fioleau and Roca, 2023)

## 1 Introduction

Deep convective systems (DCS) are central to the hydrological and energy cycle of the tropical region (Roca et al. 2014a, Roca et al. 2010). Despite a long research history (Houze, 2018), understanding the lifetime duration of tropical convective systems and the lengths of their various phases throughout their life cycles in the current climate, as well as their evolution in a warmer and moister world, remains challenging (Roca et al. 2020). Deep convective systems in the Tropics can span a wide range of scales ( $10\text{-}1000 \text{ km}$ ) and degree of organization (Houze 2004). Within this full spectrum of organized convection, Mesoscale convective systems (MCS) form a specific family of deep convective systems producing contiguous precipitation on horizontal scales larger than  $100 \text{ km}$  (Houze 2004) and which can organize into mesoscale convective complexes (Maddox, 1980), squall-line systems, super cluster (Mapes and Houze, 1993). DCS are composed of a convective core where heavy rainfall takes place, associated to a stratiform anvil with lighter precipitation as well as nonprecipitating cirriform cloudiness. DCS are further characterized by a life cycle. DCS initiate and develop from one or more individual deep convective cells, which organize themselves into convective cores. The system then enters a maturity phase in which a stratiform part and cirriform cloud expand. Finally, as convection vanishes, DCS are no longer fed by convective cells, they dissipate and scatter into several individual cirriform clouds.

Well curated global satellite observations can provide a useful resource to constraint theoretical and modelling perspectives on deep convective systems. In particular, after decades of field campaigns and detailed case studies, satellite climatology can now support the statistical analysis needed to refine our current understanding. Indeed, the information related to the life cycle of deep convective systems can only be obtained statistically at Tropical scale by using high frequency imagery available from the geostationary orbit. Meteorological agencies around the world successfully operate geostationary satellites for more than four decades.

From the 1980's, and in the context of campaign measurements (GATE, WMOMEX...), some automatic tracking algorithms have been developed and implemented for the detection and tracking of convective systems from infrared (IR) imagery of

geostationary satellites. Tracking algorithms are generally based on two steps: a detection step to identify contiguous areas of  
60 cold temperatures in a single IR image, referred to as cloud clusters in which deep convection is organized, and a tracking step  
to match the identified cloud clusters from one frame to the next. A deep convective system through its life cycle then  
corresponds to a succession of cloud clusters in a time sequence of IR images. Tracking algorithms have evolved over time in  
line with the way to describe deep convective systems, with the improvements in geostationary imagers and with the technical  
advances allowing an improvement of the identification and tracking of deep convection and their high cold cloud shields.

65 The detection stage is historically based on the thresholding of the IR images using brightness temperature (BT) thresholds to  
delineate the cloud clusters. In the literature, a wide range of temperature thresholds from 208 K to 253 K has been used to  
detect cloud clusters at different degrees of organization. Hence, Williams and Houze (1987) identified cloud clusters larger  
than 5000 km<sup>2</sup> with a 213 K threshold, while Maddox (1980) applied a 241 K threshold to identify the high cold cloud shield  
associated to Mesoscale Convective Complex (MCC) over the central United States. Machado et al (1992) studied the  
70 dependence of cloud cluster size on the choice of brightness temperature threshold for different tropical regions. They found  
that temperature thresholds in the range [240 K-255 K] had little effect on the surface of the cloud clusters. Over the years,  
developments have been made on the detection stages to improve the characterization of cloud clusters. Thus, Mathon and  
Laurent (2001) identified cloud clusters larger than 5000 km<sup>2</sup> by applying three different temperature thresholds to the infrared  
imagery: a 213 K temperature threshold to discriminate deep convective cores, a 233K threshold commonly used to estimate  
75 surface precipitation in the tropics (Arkin, 1979) and a 253 K threshold to identify the boundaries of the high cold cloud shield.  
In this way, it is possible to access the number of convective cores included in a high cloud shield. This technique has been  
adopted by Evans and Shemo (1996) and Ocasio et al. (2020) with some slightly different brightness temperature thresholds.

However, detection step based on single brightness temperature thresholds face some difficulties to catch the complexity of  
the full spectrum of convective organization (Fiolleau and Roca, 2013a). A single BT threshold tends to identify cloud cover,  
80 but cannot differentiate the components that make up convective systems. To improve the high cold cloud segmentation, Boer  
and Ramanathan (1997) have developed an algorithm called Detect And Spread (DAS). It relies on the assumption that pixels  
adjacent to a convective core in an IR satellite image belong to the same physical cloud cluster, and that the optical depth of  
cloud cover decreases from the convective core to the edge of the cloud cluster. The algorithm is based on a region growing  
technique consisting in the application of multi brightness temperature thresholds on the IR images to identify the convective  
85 cores which are then spread to reach the boundaries of the cloud shield. Similar approaches have been adopted by Roca and  
Ramanathan (2000), Feng et al. (2021) , Heikenfeld et al. (2019) , Wilcox (2003), Rajagopal et al. (2023), Autones and  
Moisselin (2013).

Regarding the tracking step, Williams and Houze (1987) introduced the area-overlapping technique to link cloud clusters in  
successive images, building the convective systems from their initiation to their dissipations. This technique has been widely  
90 used for years (Arnaud et al. 1992; Mathon and Laurent 2001 ;Machado et al. 1998), and has been the subject of numerous

technical evolutions to increase the matching accuracy between clusters identified in two successive time steps. Hence, to enhance the cloud matching, the projection of the cloud position has been added in some tracking methods (Ocasio et al. 2020, Feng et al. 2023). Huang et al. (2018) combined a Kalman filter technique with the area-overlapping method to improve the tracking of small and fast-moving convective systems. Some algorithms have based their tracking stages on a search radius method and on the prediction of the position of the cloud cluster's center of mass to link cloud clusters to each other (Heikenfeld et al. 2019, Woodley et al. 1980, Ostlund 1974). Carvalho and Jones (2001) and Endlich and Wolf (1981) used the maximum spatial correlation between cloud clusters of successive images, when Hodges (1994) has developed a minimization of cost function to improve the cloud cluster correspondence issue between two-time steps.

However, tracking algorithms based on the two-step technique (detection step and tracking step) can result in artificial splitting and merging artefacts throughout DCS life cycles that require specific post-processing (Feng et al. 2021, Williams and Houze 1987, Mathon and Laurent 2001), and which remain a major source of uncertainty when considering DCS life cycle analysis (Prein et al., 2024).

To overcome these issues, another branch of algorithms has then been developed based on the assumption that convective systems can only be tracked if they are considered as 3-dimensional (space+time) objects in their space-time domain. These algorithms do not work anymore IR image per IR image, but process a volume of IR images in 3 dimensions (longitude, latitude, time), to identify and track convective systems in a single step. Some algorithms then apply a single brightness temperature threshold in the spatio-temporal domain to detect and track deep convective systems (Mapes et al. 2009, Dias et al. 2012, Prein et al. 2024, Poujol et al. 2020). Other tracking algorithms use a more complex technique and apply a 3D multi-step, multi-thresholding technique, derived from the detect and spread method (Boer and Ramanathan, 1997), on the volume of IR imagery (Fiolleau and Roca 2013a, Jones et al. 2023). With such a 3D segmentation technique, high cold cloudiness is decomposed in deep convective systems which are not impacted by splitting and merging events as for previous tracking algorithms. At the beginning of the DCS life cycle, the individual convective cells which develop, are part of a same DCS, and feed its anvil. Similarly, at the end of DCS life cycle, the scattered cirriform clouds all belong to the same DCS which produced them.

These tracking algorithms have given rise to a large corpus of literature at the regional scale but only a few deep convective systems databases have been made available at global scale so far based on various global infrared archive (Table 1). These climatologies provided an initial perspective at tropical scale, revealing the ubiquity of mesoscale systems with various durations and spatial extents across a wide spectrum of large-scale environments. This insight has prompted numerous scientific investigations. For instance, Elsaesser et al. (2022) investigated the growth rate of the cloud shield across the entire tropical belt. Using the CLAUS dataset, the statistics of DCS triggering revealed the strong link to orography while spectral analysis brought observational support to tropical dynamics theory (Dias et al., 2012). The overwhelming contribution of the long-lasting systems to the tropical precipitation total amount was quantitatively estimated (Roca et al., 2014) as well as to the

extreme precipitation (Roca and Fiolleau, 2020). The recent decades tropical trends in precipitation has been shown to be associated with the trends in the occurrence of deep organized systems (Tan et al., 2015). These examples are strong incentive to build and sustain IR derived database of the DCS morphology in support of climatological investigations of the tropical water cycle (Feng et al., 2021).

IR source	External source	Period	Coverage	resolution		Homogenization across the fleet					algorithm technique		Reference
				Space	Time	Spatial res.	Temp res.	Spectral	Inter-calibration	VZA correction	Detection technique	Tracking technique	
<i>ISSCP-B3</i>	<i>No</i>	<i>1983-2009</i>	<i>55°S-55°N</i>	<i>30km</i>	<i>3h</i>	<i>yes</i>	<i>yes</i>	<i>No</i>	<i>yes</i>	<i>no</i>	<i>Single BT threshold</i>	<i>area-overlapping</i>	<i>(Machado and Rossow, 1993) (Vant-Hull et al., 2016)</i>
ISCCP-B3	No	1989-1993	40°S-40°N	30km	3h	Yes	Yes	No	Yes	no	Single BT threshold	area-overlapping	(Tsakraklides and Evans, 2003)
<i>CLAUS</i>	<i>No</i>	<i>1985-2008</i>	<i>30°S-30°N</i>	<i>30km</i>	<i>3h</i>	<i>yes</i>	<i>yes</i>	<i>No</i>	<i>yes</i>	<i>yes</i>	<i>Single BT threshold</i>	<i>Kalman filter combined with area-overlapping</i>	<i>(Huang et al., 2018)</i>
CLAUS	No	1985-2008	30°S-30°N	30km	3h	yes	yes	No	yes	yes	3D clustering technique	area-overlapping	(Dias et al., 2012)
Gridsat	IBTrACS	1980-2008	Tropical oceanic basins	8km	3h	Yes	Yes	No	Yes		Single BT threshold	area-overlapping	(Hennon et al., 2013)
CPC Mosaic	No	2002-2012	60°S-60°N	4km	30'	Yes	Yes	No	No	Yes	Single BT threshold	area-overlapping	(Esmaili et al., 2016)
GEO Raw data	No		60°S-60°N			No	No	No	No	No	Single BT threshold	area-overlapping	(Laing and Fritsch 1997)
GEO Ring Raw data	No	Summer 2012-2014	30°S-30°N	2 to 5km	30'	No	Yes	No	None	None	3D Detect And Spread (TOOCAN)		(Roca et al. 2017)
<i>CPC Mosaic</i>	<i>iMERG IBTrACS</i>	<i>2001-2019</i>	<i>60°S-60°N</i>	<i>0.1°</i>	<i>1h</i>	<i>yes</i>	<i>yes</i>	<i>No</i>	<i>None</i>	<i>Yes</i>	<i>Detect And Spread</i>	<i>area-overlapping</i>	<i>(Feng et al., 2021)</i>
GEO Ring Raw data	No	2012-2016	30°S-30°N	0.04°	30'	Yes	Yes	Yes	Yes	Yes	3D Detect And Spread (TOOCAN)		(Bouniol et al., 2021) (Elsaesser et al., 2022)

**Table 1** Technical characteristics of the existing DCS databases over the entire tropical band. The DCS databases made available and associated with a DOI are indicated in *italic*

On the other hand, the limitations of the IR information to document the precipitating processes occurring at the sub storm scale are well known (Liu et al., 2007) yet the IR based convective cloud shield analysis can shed significant insights into the dynamics of the system. A simple two stages model can well describe the life cycle of the DCS shield and that the morphological parameters of the storms are so tightly related that eventually the full life cycle of the cloud shield can be reconstructed knowing for instance only the duration and the maximum extension of the system (Roca et al., 2017). IR derived information about the DCS life are crucial to contextualize overpassing observations, be it active or passive microwave observations (Fiolleau and Roca 2013b, Bouniol et al. 2016). The knowledge of the cloud shield can further inform physically based precipitation retrievals (Bellerby et al. 2009, Guilloteau and Foufoula-Georgiou 2024). Such variety of applications is one more strong motivation to elaborate upon the infrared archive to document the life cycle of DCS in support of process studies.

Cloud tracking algorithm further add requirements to the GEORing<sup>1</sup> dataset used to elaborate global MCS climatology. While  
140 a few studies rely on 3 hourly data, it is important to make use of at least 30 minutes imagery to describe the full spectrum of  
deep convective systems (Fioleau and Roca, 2013a). Similarly, high resolution observation is required to address the full life  
cycle of the convective systems that could otherwise be truncated (Schröder et al., 2009). The variety of spatial and spectral  
resolution for instance for the period 2012-2020 (see discussion below) further calls for a homogenization effort at the level 1  
prior to running the tracking algorithm (Fioleau et al., 2020).

145 This paper presents such a DCS database built from a homogenized IR archive and a tracking algorithm called TOOCAN  
(Tracking Of Organized Convection Algorithm using a 3-dimensional segmentationN) (Fioleau and Roca, 2013a). In Section 2,  
we present the harmonized infrared geostationary dataset, and the way we have performed the homogenization procedure using  
the ScaRaB-Megha-tropiques IR observation. We will then introduce the IBTrACS dataset, which will be used to filter out  
DCS belonging to a cyclonic circulation or if these DCS are classified themselves as cyclonic events. The functioning of the  
150 TOOCAN algorithm is introduced section 3. We will discuss the possible uncertainty on the deep convective systems  
occurrences and characteristics induced by the residual error of the homogenization procedure, as well as the geostationary  
data availability. Exemplary illustrations of the database are shown in section 4 and finally, the data availability and format  
are further discussed in Section 5.

## 2 Data

### 155 2.1 The harmonized infrared geostationary dataset 2012-2020

Thermal channel brightness temperature data obtained by the operational meteorological geostationary satellite fleet are used  
to monitor the deep convective systems over the tropical belt for the whole 2012-2020 period. Table 2 shows the technical  
characteristics of the fleet of geostationary platforms (GEORing) and their associated IR channels over the 9-year period. As  
shown in Fioleau et al. (2020), the GEORing is far from a homogeneous suite of instruments operated in similar fashion.  
160 Spatial and temporal resolutions, as well as the spectral filter functions and the calibration procedures differ from one platform  
to another. All of these technical differences lead to biases in the brightness temperature measurement from one geostationary  
platform to another one. To overcome such issues, Fioleau et al. (2020) have then developed a methodology of homogenization  
of the thermal infrared channels of the meteorological geostationary satellite fleet for cold cloud studies and based on the IR  
channel of the Scanner for Radiation Budget (ScaRaB) onboard Megha-Tropiques. This homogenization procedure includes  
165 the computation of the inter-calibration and spectral normalization coefficients every 10 days as well as the correction of the  
limb darkening effects impacting the brightness temperature measurements in the range [180K-240K] from geostationary  
satellites for the 2012-2016 period. The extension of the geostationary database until 2020 has required to continue this

---

<sup>1</sup> The GEORing refers to the whole geostationary platforms which data all together covers all the longitude of the Earth surface.

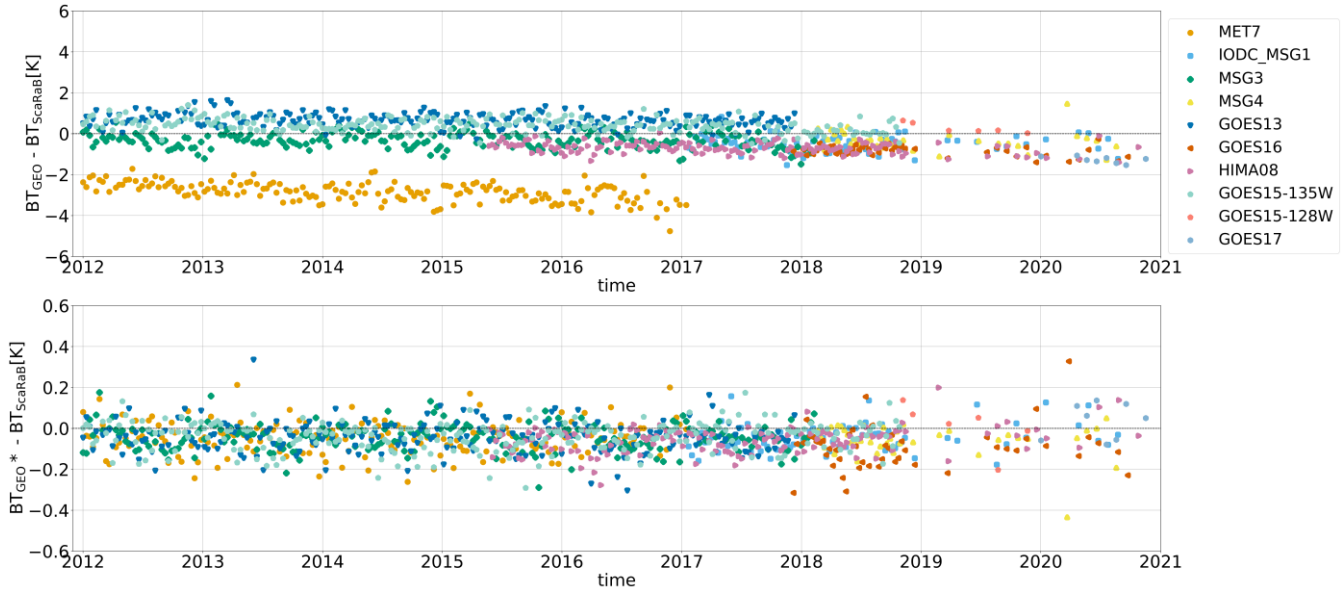
170 harmonization effort. These four additional years are characterized by the launch of new geostationary satellites. Over the Indian ocean, METEOSAT-7 has been replaced by MSG-1 in January 2017, the new generation GOES-16 has replaced GOES-13 over Americas in December 2017. Finally, over the Eastern Pacific region, the GOES-15 platform has been shifted from its initial nadir at 135° W to 128° W in November 2017 to ensure continuity of observations in the Eastern Pacific before being replaced by GOES-17 in December 2019. From the end of 2018, the Megha-Tropiques satellite suffers from technical issues on the data management subsystem, implying a decreasing of the availability of the ScaRaB data. From this date, only about 30% of the data are available. Nevertheless, the quality of the ScaRaB measurements is not impacting by such technical issues, and have the same performance as at the beginning of the mission. To overcome the lack of ScaRaB observation, the calculation of inter-calibration and spectral normalization coefficients was carried out every 30 days instead of the initial 10 days.

Region	Platform	Nadir location	Instrument	Central wavelength	Spectral interval	Spatial resolution at nadir	Temporal resolution	Spatial coverage	Source	Period
EASTERNPACIFIC	GOES-15	135°W	IMAGER	10.7 $\mu\text{m}$	10.2-11.2 $\mu\text{m}$	4 km	30 min	180°W-105°W 55°S-55°N	NOAA/DWD	01/2012-11/2017
EASTERNPACIFIC	GOES-15	128°W	IMAGER	10.7 $\mu\text{m}$	10.2-11.2 $\mu\text{m}$	4 km	30 min	180°W-105°W 55°S-55°N	NOAA/DWD	11/2017-12/2019
EASTERNPACIFIC	GOES-17	137°W	IMAGER	11.2 $\mu\text{m}$	10.4-12.0 $\mu\text{m}$	2 km	10 min	170°W-80°W 55°S-55°N	AERIS/NOAA	12/2019-12/2020
AMERICA	GOES-13	75°W	IMAGER	10.7 $\mu\text{m}$	10.2-11.2 $\mu\text{m}$	4 km	30 min	111°W-30°W 55°S-55°N	NOAA/DWD	01/2012-12/2017
AMERICA	GOES-16	75°W	IMAGER	11.2 $\mu\text{m}$	10.4-12.0 $\mu\text{m}$	2 km	10 min	130°W-20°W 55°S-55°N	AERIS/NOAA	12/2017-12/2020
AFRICA	METEOSAT-8/9/10/11	0°	SEVIRI	10.8 $\mu\text{m}$	9.8-11.8 $\mu\text{m}$	3 km	15 min	45°W-45°E 55°S-55°N	EUMETSAT/ AERIS	01/2012-12/2020
INDIA	METEOSAT-7 (IODC)	57.5°E	MVIRI	11.5 $\mu\text{m}$	10.5-12.5 $\mu\text{m}$	5 km	30 min	30°E-107°E 55°S-55°N	EUMETSAT/ AERIS	01/2012-01/2017
INDIA	METEOSAT-8 (IODC)	40.5°	SEVIRI	10.8 $\mu\text{m}$	9.8-11.8 $\mu\text{m}$	3 km	15 min	30°E-95°E 55°S-55°N	EUMETSAT/ AERIS	01/2017-12/2020
WESTERNPACIFIC	MTSAT-2	145°E	IMAGER	10.8 $\mu\text{m}$	10.3-11.3 $\mu\text{m}$	4 km	30 min	94°E-170°W 55°S-55°N	AERIS/ CIMSS	01/2012-05/2015
WESTERNPACIFIC	HIMAWARI-8	140.7°E	AHI	11.2 $\mu\text{m}$	11.0-11.4 $\mu\text{m}$	2 km	10 min	94°E-170°W 55°S-55°N	AERIS/ JMA	06/2015-12/2020

**Table 2** Technical characteristics of the operational geostationary satellites fleet and the associated imagers used over the 2012-2020 period.

180 Figure 1a shows the time series of the initial bias in BT for all the geostationary imagers with respect to the ScaRaB observation in the range [180 K-240 K], and for geostationary zenith angle lower than 20° over the 2012-2020 period. The large bias observed in the MET7/MVIRI calibration between 2012 and 2017 (Figure 1a) is explained by significant ice contamination on the MVIRI optics, as fully discussed in Hewison et al. (2013) and Fiolleau et al. (2020). The results of the inter-calibration and spectral normalization is shown Fig. 1b. Over the entire period and for all the geostationary platform, the decadal residual bias indicates a very small and stable bias ( $< 0.04$  K) with a standard deviation lower than 0.07 K between  $BT_{\text{SCARAB}}$  and the inter-calibrated  $BT_{\text{GEO}}$  ( $BT_{\text{GEO}}^*$ ). The decrease of the ScaRaB data availability does not impact the quality of the corrections from the end of 2018. The limb darkening correction is the final step of the harmonization process and is performed geostationary satellite per geostationary satellite. The method has been fully described in Fiolleau et al. (2020). Figure 2 shows

the variation of the biases of  $BT_{GEO}$  for values lower than 235K between pairs of geostationary satellites monitoring a same region according to the difference of their zenith angles ( $\Delta VZA$ ), before and after zenith angle corrections. Without any corrections,  $BT_{GEO}^*$  bias varies from -5 K to +5 K as the  $\Delta VZA$  moves from  $-50^\circ$  to  $50^\circ$  regardless the geostationary platform (Figure 2a). By applying the zenith angle correction, this bias averages 0.21 K with a standard deviation of 1.33 K throughout the GEOring, independent of the variation in  $\Delta VZA$ .



195 **Figure 1 (a)** Time series of initial BT bias of geostationary IR observations with respect to SCARAB in the range [180 K-240 K] between 2012 and 2020; **(b)** after spectral and calibration corrections.

To finalize the harmonization procedure, the temporal resolution has been unified to 30 minutes across the GEOring and all the geostationary data have been remapped into a common longitude-latitude  $0.04^\circ$  equal-angle grid (Fioleau et al., 2020). The spatial coverage of each geostationary has been chosen relatively wide in longitude to have an important overlapping area between adjacent geostationary platforms, and between  $55^\circ$  S and  $55^\circ$  N in latitude.

GOES-13 and GOES-15 sensors follow a complex scanning sectors schedule. The full disk images are produced every 3 h, while the north hemisphere and the south hemisphere images are produced every 30 minutes with a time lag of few minutes between each scan. Thus, to get a full disk image at a 30-minute temporal resolution, the southern and northern scans of GOES-13 and GOES-15 have been concatenated. The acquisition scheme of the MTSAT-1 and 2 platform (from January 2012 to May 2015) over the Western Pacific region only provides northern hemisphere imagery at a 30-minute frequency; the southern hemisphere zone is only available every hour. Similarly, the southern hemisphere of a small region between  $118^\circ$  W and  $108^\circ$  W is only monitored at a 3 h temporal resolution by GOES-15.



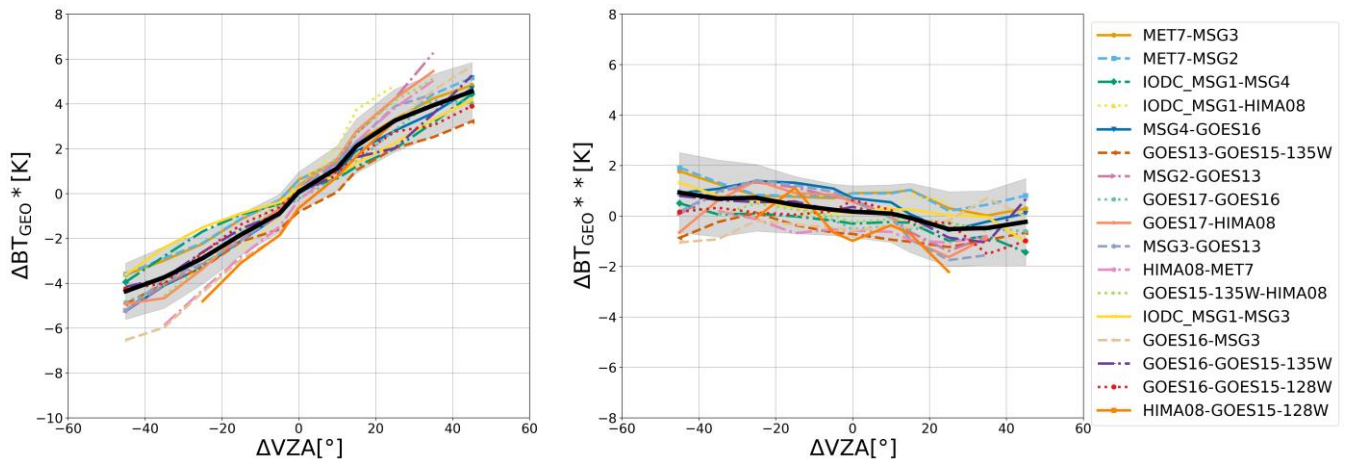
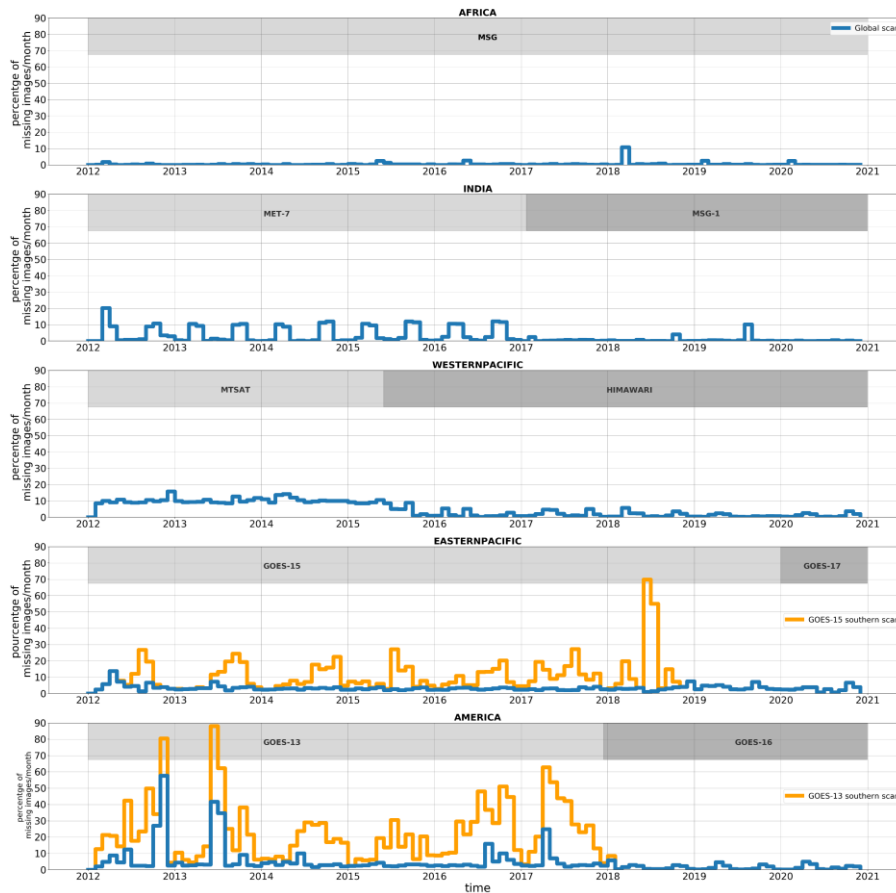


**Figure 2** (a) Variation of the BT bias according to the VZA differences between pairs of geostationary platforms observing common areas and for  $BT_{SCARAB}$  in the range [180 K-235 K] between 2012 and 2020 before Viewing Zenith Angle corrections; (b) after Viewing Zenith Angle corrections. The BT bias and its standard deviation for all the pairs of geostationary platforms are represented respectively by the black line and the filled area in grey.

Low-quality infrared images have been filtered out by applying a quality control on all the geostationary IR data (Szantai et al., 2011). Overall, the availability of all the geostationary platforms during the 2012-2020 period exceeds 96.8 % with the highest availability over Africa (99.6 %) and the lowest availability for the Western Pacific region (95 %). Figure 3 shows the time series of the missing data for all the geostationary platforms. METEOSAT-7 over India is impacted during the boreal summer by solar eclipses and data are not disseminated during a couple of hours each day from early August to mid-September and from February to March. We can notice that the replacement of METEOSAT-7 by MSG-1 in January 2017 increases drastically the data availability. Similarly, the time series highlights the improvement of data availability as the configuration of the fleet changes over time. Thus, the rate of missing data falls from 9.6 % to 1.77 % with the operationalization of HIMAWARI-8 over Western Pacific from June 2015 on-ward. The replacement of GOES-13 by GOES-16 over the American region in January 2018 improves also remarkably the data availability from 93.8 % to 98.6 %. It is also to be noticed that the new generation of the GOES platforms is not anymore impacted by rapid scan operations as was the case with older platforms, which prevented the scanning of the southern hemisphere of the American and Eastern Pacific regions. Such operation modes (orange curves) impact a high number of days during the coverage period of GOES-13 (13 % of the days) and GOES-15 (8.76 % of the days). The deployments of GOES-16 in 2018 and GOES-17 in December 2019 to their respective nadir positions over respectively the American and Eastern Pacific regions highly improve the observation of the southern regions. The overall

availability of the GEOring data over the entire period is then well suited to document the deep cloudiness in the tropical regions.



230 **Figure 3** Time series of the percentage of missing IR data per month for each region of interest and geostationary platform over the 2012-2020 period. Orange lines correspond to the availability of the southern scans of GOES-13 and GOES-15 which can be impacted by Rapid Scan Operation modes.

## 2.2 IBTrACS dataset

235 To understand the general characteristics and behavior of tropical DCS, it is important to filter out the cloud systems affected by atmospheric conditions, associated with tropical cyclones. To this end, we use the IBTrACS dataset to flag DCS belonging to a cyclonic circulation or classified themselves as tropical cyclones, allowing to either filter them out of the analysis or keep them as needed.

The International Best Track Archive for Climate Stewardship (IBTrACS) version 4 is a dataset combining all of the tropical cyclone best-track data from all the World Meteorological Organization (WMO) Regional Specialized Meteorological Centers

240 (RSMCs), as well as other national agencies (e.g., the Joint Typhoon Warning Center) over the globe (Knapp et al., 2011). The dataset contains the tropical cyclone location, maximum sustained wind (MSW) and minimum central pressure (MSP) as well as additional information depending on the forecast center every 6h along the lifetime of the tropical cyclone. The tropical storm positions are interpolated in time to 3 hourly positions. In this study, we will determine whether a deep convective system is closed to a tropical cyclones meteorological event at 00h00 UTC, 06h00 UTC, 12h00 UTC, and 18h00 UTC. The combination procedure between convection systems and tropical storms is described in section 3.3. The WMO standard for MSW is a 10-min average (WMO 1983), which is used at many of the forecast centers. However, some forecast agencies use a different temporal average for MSW. A 1-min average for MSW is used at the United States forecast centers (JTWC, NHC, and CPHC), a 2-min average at the Chinese Meteorological Administration's Shanghai Typhoon Institute, and a 3-min average used at the India Meteorological Department. A conversion of all MSW to a common temporal average is then required to analyze statistically tropical cyclone over the tropics and several conversion factors have already been determined by Harper et al. (2008). For our study, we will use the same factor 0.88 than the one used in (Kruk et al., 2010) to convert all the basins' MSW to a 1-min average. The MSW is then used to classify all the tropical cyclones according to the Saffir-Simpson hurricane wind scale (SSHS). Over the 2012-2020 period, 825 meteorological events are classified as tropical storms. Among them, 410 tropical cyclones have been identified. 208 of them have reached the SSHS category 3 (90 kt) during their lifetime, 142 the SSHS category 4, and 17 the SSHS category 5 (136 kt).

### 3 TOOCAN algorithm

#### 3.1 The principle

The functioning of the TOOCAN (Tracking Of Organized Convection Algorithm through a 3-D segmentation) algorithm has been fully described and explained in Fiolleau and Roca (2013a). The algorithm relies on a conceptual model of a convective system consisting in an initiation phase in which deep convective cells develop and organize in a convective core, a maturity phase in which an anvil cloud develops associated to its convective core followed by a dissipation stage, in which no more convection occurs and the system breaks up into multiple cirriform clouds. Both in the spatial and temporal domains, the optical depth of cloud cover decreases from the convective core to the edge of the anvil cloud, as the brightness temperature increases. This conceptual model of a convective system corresponds then to a 3D (longitude, latitude, time) cloud cluster made up of a convective core associated to its stratiform anvil and cirriform clouds evolving in the space-time domain.

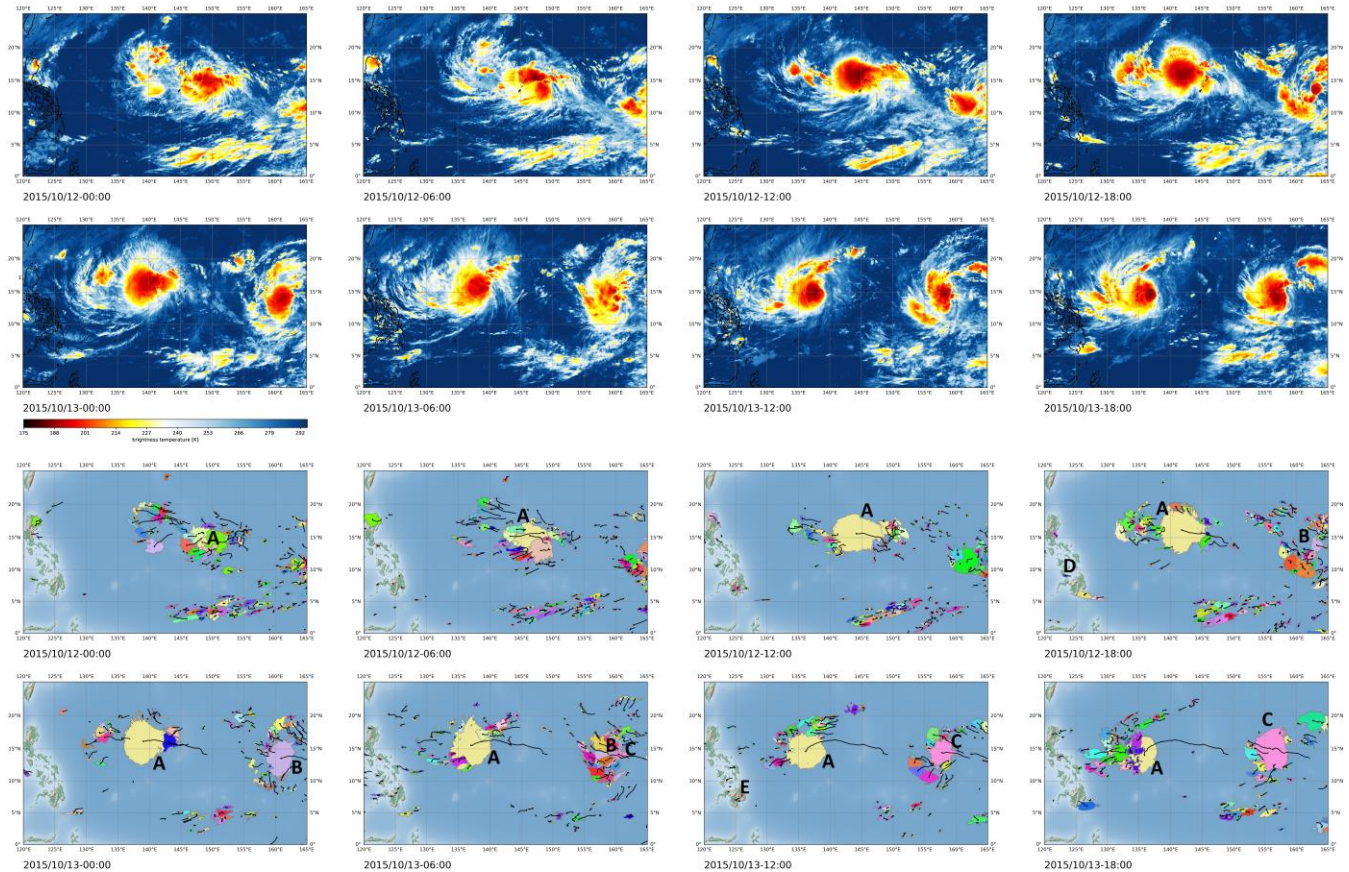
To identify such a 3D-cloud cluster, the algorithm works within a time sequence of IR images, and applies a 3-D region growing technique, to decompose the high cold cloud shield, defined by a 235 K threshold in the spatio-temporal domain into component DCSs. This technique consists in an iterative process of detection and dilation of convective seeds in the spatio-temporal domain to detect and track DCS in a single 3D segmentation step. Individual convective seeds are first detected by applying a cold brightness temperature threshold set at 190 K on the volume of IR images. If any, convective seeds with a minimum lifetime duration of 3 frames (1h30) and exceeding 625 km<sup>2</sup> per frame are kept and are spread in the spatio-temporal

domain until reaching the intermediate cold cloud shield boundaries identified at a 2K warmer BT threshold. This dilation step involves adding pixels belonging to the intermediate cold cloud shield to all previously detected convective seeds using a 10-connected spatiotemporal neighborhood kernel operator, composed of an 8-connected spatial neighborhood and a 2-connected temporal neighborhood, to favor spatial spread over temporal spread. The pixel aggregation process is constrained by a brightness temperature difference between the edge pixels and the already identified pixel, which has to be greater than -1 K to minimize the effects of local minima. Then, a new detection is applied at the 192 K threshold to detect the convective seeds too warm to be identified at the previous Tb threshold (190 K). If any, all the convective seeds are then spread until reaching the intermediate cold cloud shield boundaries at a 2 K warmer BT threshold (194 K). This iterative process of detection and dilatation is repeated with a 2K detection step from 190 K to 235 K and is stopped when all the pixels below 235K are associated with a DCS. The very cold 190 K threshold is required to identify very deep convective cores which occur in the Tropics. The multi-BT thresholds between 190 K and 235 K allows to identify the wide variety of convective cores which occur and may be more or less deep. Thanks to its spatio-temporal region-growing technique, the TOOCAN algorithm can track DCS by suppressing split and merge artifacts throughout their life cycles, which are inherent to classic overlap-based tracking techniques.

The first spatio-temporal volume of IR images is built by accumulating 15 days of geostationary infrared data in which TOOCAN operates. TOOCAN is applied in the next 15-day of volume images with a sliced-window technique, allowing a continuity of the tracked DCS between the 2 successive spatio-temporal volumes. With regard to big data processing, the algorithm can face missing IR data. When low-quality or missing images are encountered in the time series, the data available at previous and subsequent time steps are replicated, so that the tracking is carried out nominally, enabling continuity of the deep convective cloud life cycle. However, beyond a given number of successive missing images, the TOOCAN process has to be stopped, and a fresh start has to be operated at the end of the interruption. DCS impacted by this interruption are all terminated and new systems are considered to initiate at the end of the interruption, causing artificial life cycles and some biases in lifetime duration distributions. Section 3.2b will detail the sensitivity of the DCS characteristics to the data availability.

Figure 4a and 4b show a time series of the TOOCAN segmented images from the HIMAWARI-8 IR data between 12<sup>th</sup> October 2015 at 0h00 UTC and 13<sup>th</sup> October 2015 18h00 UTC over the Western Pacific Ocean. The high cold cloud shield defined by a 235 K threshold on the infrared imagery is decomposed into several deep convective systems whose anvil clouds touch each other. The full spectrum of deep convective systems organization is identified ranging from small, short-lived and isolated systems to long lasting systems, reaching several thousands of kilometers per square meters and propagating over several hundred kilometers. For instance, the deep convective systems A and C identified over the Pacific Ocean on the time series last 60 h and 137 h respectively, reach a cold cloud surface larger than  $4.5 \times 10^5$  km<sup>2</sup>, and propagate on a distance greater than 2000 km. The convective system B, has a lifetime duration of 22.5 h with a  $2.5 \times 10^5$  km<sup>2</sup> maximum extent and propagates Westward over 890 km. All these very large and long-lived convective systems belong and contribute to complex convective

305 situations, sharing common high cloud cover with various convective systems that exhibit a wide range of morphological characteristics, with which they interact. Other convective systems are more isolated during their life cycles. This is the case of the DCS D and E over the Philippines islands which last ~4 h and reach a maximum cold cloud surface of ~5500 km<sup>2</sup>. These systems are also characterized by their relatively stationarity, and exhibit a propagating distance of 123 km and 74 km, for DCS D and E respectively.



310

**Figure 4** Illustration of the TOOCAN segmentations for a convective situation which occurred in October 2015, over the Western Pacific region, which is also presented as Video S1 in the supplement (Fioleau, 2024). (a) Infrared observation of HIMAWARI-8 every 6h from 12 October 2015 at 00:00 UTC to 13 October 2015 at 18:00 UTC; (b) DCS segmented by the TOOCAN algorithm. Each color corresponds to a unique deep convective system. The black lines indicate the trajectories of their centers of mass since initiation.

315

### 3.2 Uncertainty estimation

In this section, we will focus on assessing the impact of radiometric errors and missing images on the performance of the segmentation and tracking of deep convective systems from IR imagery as well as on the error propagation in statistical analyses of DCS.

#### 320 3.2.a Uncertainty estimation due to radiometric errors

As discussed in section 2.1, IR observation have been homogenized with an error lower than 1.5 K throughout the GEOring considering the inter-calibration, spectral normalization and limb darkening corrections. In the following, we assess the impact of such a residual error on the morphological characteristics and occurrences of the DCS. For that, the analysis is based on the MSG IR dataset over the June to September 2012 period over the  $40^\circ$  W- $40^\circ$  E;  $30^\circ$  S- $30^\circ$  N region.

325 From this reference dataset, we have produced an ensemble of 134 MSG-1 IR datasets over the same region and period, whose brightness temperatures have been biased by a value estimated from a gaussian distribution with a 1.5 K standard deviation (Figure 5). The TOOCAN algorithm has been applied on these 134 biased MSG IR datasets in order to produce an ensemble of different DCS segmentations. The average distribution of the DCS lifetime durations computed from the ensemble of MSG IR dataset (blue line) shown in Fig. 6 indicates that maximum of population occurs for systems lasting in the range 0-5 h with  
330 around  $3 \times 10^4$  DCS. Then, the DCS population decreases as the lifetime duration increases. In average, around 320 DCS last more than 20 h on the 134 runs of TOOCAN.

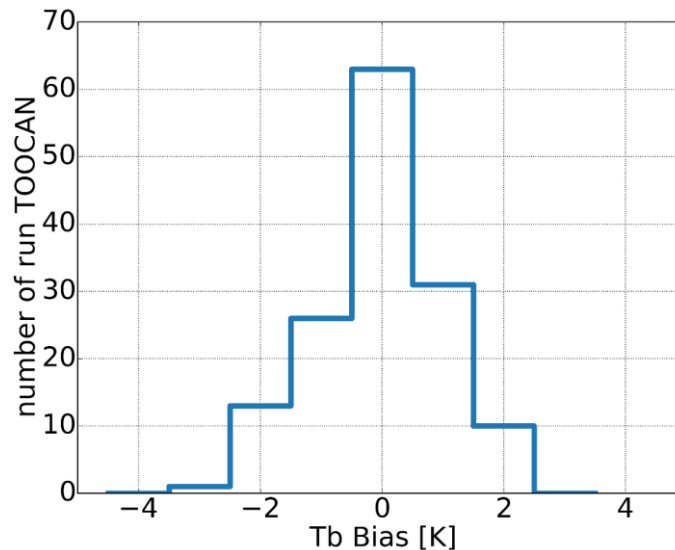
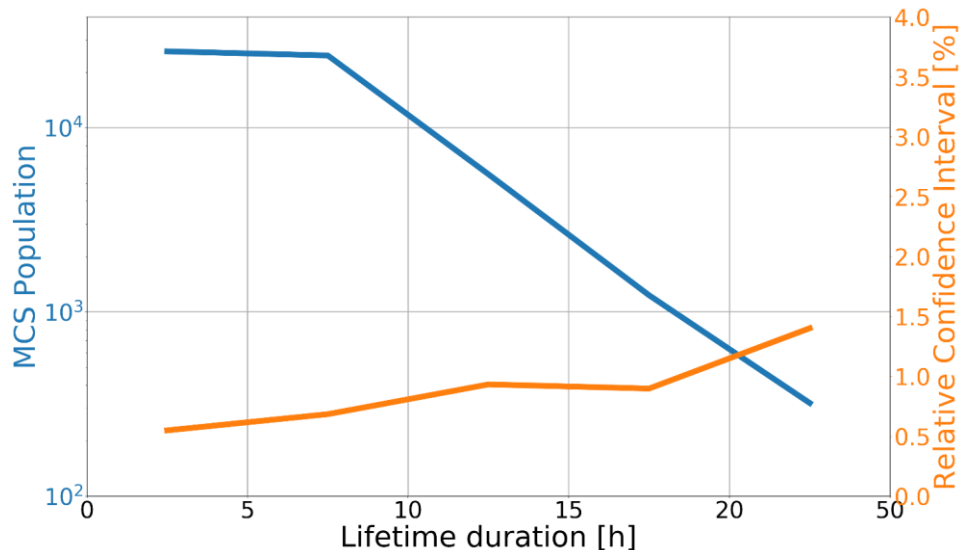


**Figure 5** Distribution of the brightness temperature bias applied on the MSG dataset between June to September 2012 and which has been built from a gaussian distribution with a 1.5K standard deviation.

335 The relative confidence interval (orange line) is shown Fig. 7 as a function of the lifetime duration and is computed as the absolute 95 % confidence interval divided by the DCS averaged occurrence multiplied by 100 %.



340 **Figure 6** Distribution of the average DCS lifetime duration (blue curve) computed from the 134 perturbed runs of TOOCAN applied on IR imagery of MSG from June to September in 2012 over the 40°W-40°E;30°S-30°N region and the associated relative confidence interval (orange).

This sensitivity study reveals a small relative confidence interval whatever the bins of lifetime duration. For systems lasting less than 5h, a 0.54 % relative confidence interval is observed for a population of ~26000 DCS, meaning that we are 95 % confident that the true DCS population < 5 h is between 25859 and 26240 with a 1.5 K residual error. This relative confidence interval increases slightly as the lifetime duration increases and DCS population decreases. However, the relative confidence interval remains relatively weak with a value ~1.40 % for DCS lasting more than 20 h. For these long-lasting systems, the absolute confidence interval of the DCS population is between 315 and 320.

Given the assumed 1.5 K residual bias throughout the GEOring, this analysis has shown that the IR segmentation and the DCS tracking by the TOOCAN algorithm as well as the resulting DCS lifetime duration distributions are not sensitive to such an error source.

### 350 3.2.b Uncertainty estimation due to the IR geostationary data availability

The sensitivity of the DCS morphological parameters is now evaluated according to the availability of the IR geostationary images. From the point of view of cloud tracking, the major problem lies less in isolated missing data than in the number of successive missing images over time, which have an impact on the continuity and quality of cloud tracking. As seen previously in section 3.1, if any missing images are found in the time series, they are replaced by the data available in the previous and

355 following time steps, allowing convective systems to be tracked. It is then important to assess the impact of consecutive missing images on the statistics of the DCS occurrence, and on the characterization of their morphological parameters.

Several scenarios arise for the DCS facing such a time period of consecutive missing images. DCS that were supposed to initiate during this missing data gap are either detected at the time of resumption, in which case their duration is artificially shortened, or they cannot be identified at all. DCS that were supposed to dissipate during this period of missing images could  
360 dissipate at the time of resumption, in which case their lifetime duration is artificially extended. There is the case of DCS that started before the series of missing images and are expected to persist thereafter can still be tracked despite this interruption. Some DCS cannot survive the period of missing data and then dissipate artificially. Smaller systems may not survive this interruption, reducing their lifetime, or their lifetime may be artificially extended due to data replication.

Also, this sensitivity study will help us to determine the threshold on the number of successive missing images beyond which  
365 the DCS parameters are too degraded, so that the TOOCAN process has to be interrupted.

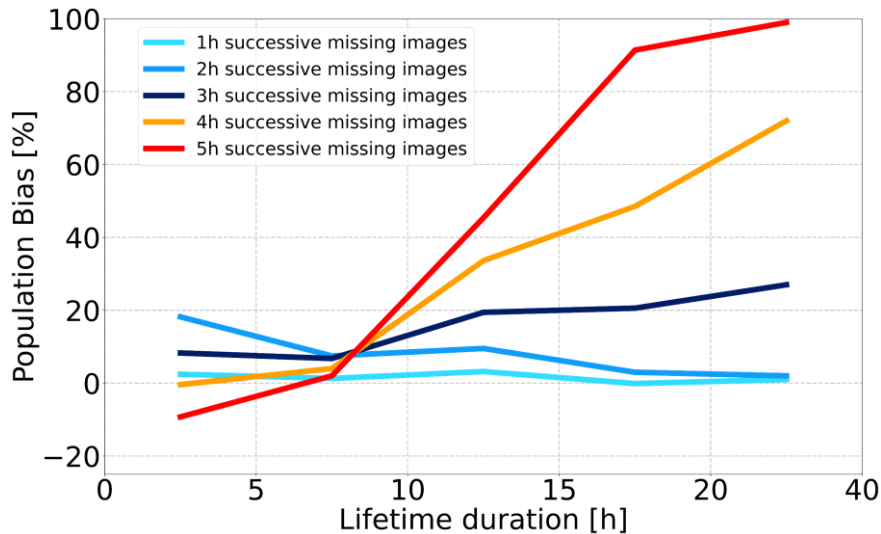


**Figure 7** Bias on the DCS population according to the lifetime duration between a reference run of TOOCAN applied on a complete MSG IR dataset in June-September 2012 over the 40°W-40°E; 30°S-30°N region and five runs of TOOCAN applied on similar MSG IR dataset but degraded every day with 1h, 2h, 3h, 4h and 5h successive missing images.

The same MSG IR observations over the African and Atlantic region from June to September 2012 constitute our baseline for  
370 this analysis. This database is characterized by no missing data over the study period (Figure 3). To better understand the impact of the missing data periods on the DCS parameters, the TOOCAN algorithm is first applied on this reference MSG IR database, and then is applied on this same database but degraded by deleting everyday 1h of consecutive images (between 19:00 UTC and 20:00 UTC), 2h (between 19h00 UTC and 21h00 UTC), 3h (between 19h00 UTC and 22h00 UTC), 4h (between 19h00 UTC and 23h00 UTC) and finally 5h (between 19h00 UTC and 00h00 UTC) of consecutive images. The  
375 missing data periods are filled by duplicating the available MSG IR data just before and after the missing data gap.



We have focused our analysis on the late hours of each day to mimic the MFG eclipse seasons, during which consecutive missing data occur in the evening. A gap of successive missing data in the afternoon would be more impactful on the DCS population than at night, due to the diurnal cycle of initiation. However, our aim here is to determine the duration of consecutive missing data beyond which tracking the longest-lived and largest DCS becomes ineffective, leading to degraded statistics for these systems.

Figure 7 shows the bias of DCS occurrences according to their lifetime duration between the five degraded runs of TOOCAN and the TOOCAN reference run. Up to 2 h of consecutive missing images, results indicate a bias which tends toward 0 % for the longest ones. For a run performed with 3 h of consecutive missing images, we observe an over-estimation of the DCS occurrences around 20 % for systems longer than 10 h. The biases on DCS occurrences increase drastically with the 4 h and 5 h consecutive missing images, and we observe an over-estimation of DCS occurrences greater than 80 % and 100 % respectively for long DCS lifetime durations. A maximum of 3 h of consecutive missing images therefore seems to be a good compromise for ensuring tracking continuity and minimizing the impact on DCS morphological parameters of longest-lived systems. Note that here by perturbing every day the dataset, we are exploring the worst-case scenario similar to the MFG eclipse' seasons.

### 3.3 TOOCAN Implementation

The TOOCAN algorithm has been applied on the harmonized infrared observations of each geostationary platform at a 30min temporal resolution from January 2012 to December 2020. The spatial coverage of each monitored region described table 2 is wide enough in longitude to offer an overlapping area with its neighbor's regions and is extended from 40° S to 40° N in latitude to avoid an impact of the image boundaries on the tracking of DCS over the tropical belt. Applying a minimum buffer strip of 5° from the minimum/maximum geographical coordinates of these extended regions, ensure that the shape and trajectories of convective systems identified in the tropical belt are not impacted by the image boundaries.

The time series of the number of days per month impacted by 1 h, 2 h, 3 h and more than 3 h successive missing images over the 2012-2020 period is presented Fig. 8 for each geostationary platform and region of interest. During this period, 1.5 % of days are impacted by consecutive missing data lasting more than 3h over the entire tropics and for all the geostationary platforms. From 2012 to 2017, METEOSAT-7 is the most strongly impacted by consecutive missing data especially from early August to mid-September and from February to March which is explained by solar eclipses. During these periods, more than 5.8 % of the days are impacted by a maximum of 3 h consecutive missing images and 0.73 % by a sequence of more than 3 h consecutive missing images. From the analysis carried out in section 3.2.b, we define a maximum of 3h consecutive missing images, above which the tracking of DCS will be stopped. This duration of missing images is a good trade-off to track convective systems with a reasonable statistical bias on their occurrences as seen previously but also with a limited number of days impacted by such successive missing data events.

410 Finally, in order to have a homogeneous analysis of DCS thereafter, the tracking process is not carried out on the southern scan of the MTSAT-1 and 2 platform from January 2012 to May 2015, as the 30-minute time-frequency requirement is not fulfilled. For similar reason, TOOCAN is not applied on a little region between 118° W and 108° W in the southern hemisphere which is monitored by GOES-15 only every 3 h.

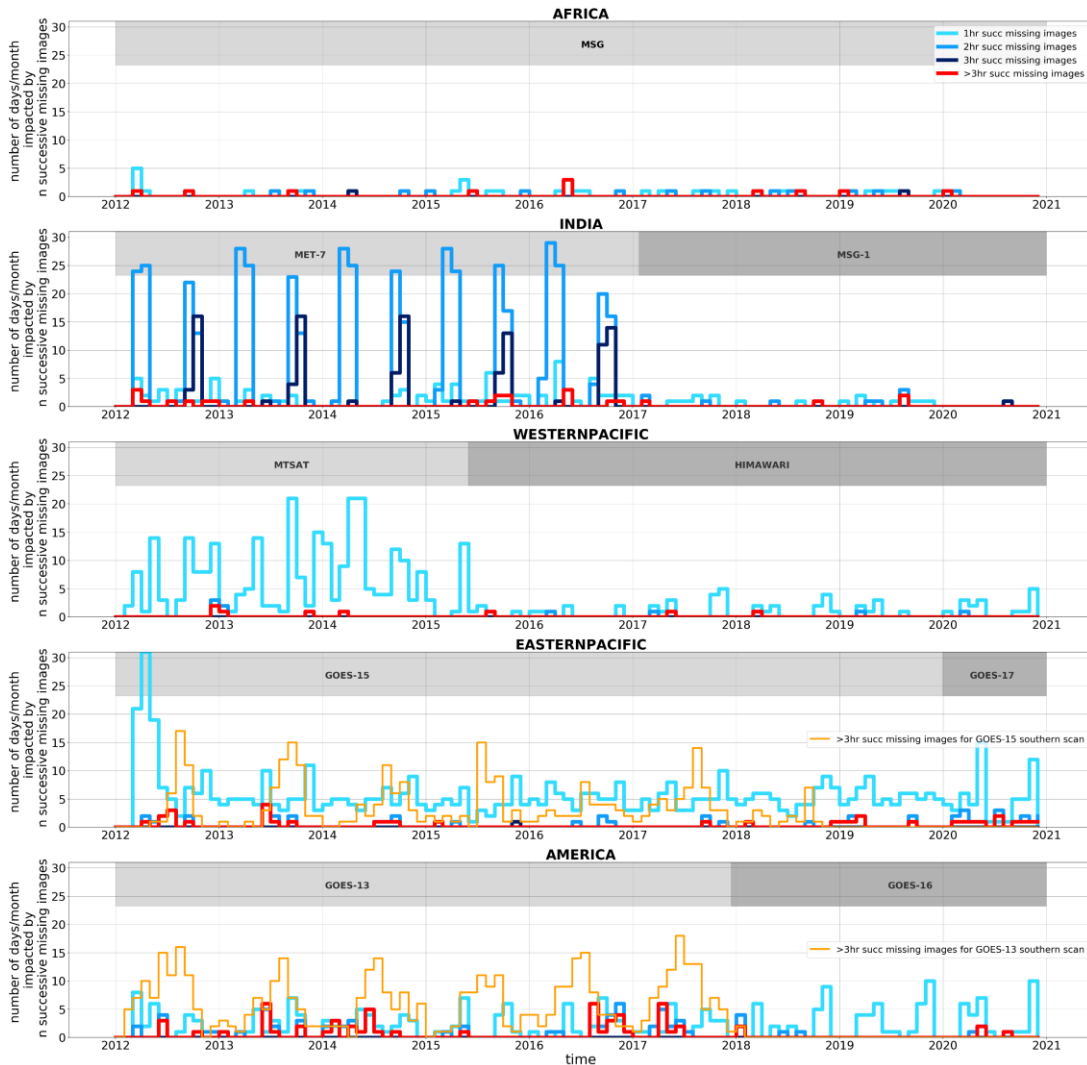


**Figure 8** Time series of the number of days per month impacted by 1h, 2h, 3h and more than 3h successive missing images between 2012 and 2020 and for the 5 regions of interest. The grey shading indicates the operability period for each geostationary platform.

## 4 The TOOCAN and the CACATOES datasets

### 415 4.2 TOOCAN dataset

The processing has given rise to a 9-year of DCS database documenting convective systems identified over the tropical belt. From one side, the dataset documents the integrated morphological parameters of each identified DCS (Table B1). On the other side, the morphological properties of each convective system are described every 30 minutes along their life cycles (Table B2). Quality control can raise a number of issues with the data, such as missing lines or images which can affect the tracking of systems in various ways. The user is informed of the issues thanks to a flag coded as a five digits number. The first digit indicates whether a DCS is born naturally or due to consecutive missing images, while the second digit indicates whether a DCS dissipates naturally or as a result of consecutive missing images. The third digit reveals if a DCS is impacted by the edges of the image, some missing lines or pixels. Values of these three digits greater than one indicate problems in initiation, dissipation, missing lines or touching the edge of the image. The last two digits of the quality flag represent the number of missing images during the lifecycle of a given DCS. A typical conservative filtering approach would include only systems unaffected by quality control issues, identified by a flag value less than 11110.

Each cloud system has received a unique label and the documentation of the convective systems has also been enhanced with some classifications. First, convective systems have been classified following the three categories of systems introduced in Fiolleau and Roca (2013a) and Roca et al. (2017a). The Deep convective systems are also categorized according to their organization, their shapes at small and large scales. In an identical way to the categories introduced by Maddox (1980) and Jirak et al. (2003), DCS are then classified into four types as Mesoscale Convective Complex (MCC), Persistent Elongated Convective System (PECS), Meso- $\beta$ -Circular Convective System (M $\beta$ CCS), and Meso- $\beta$ -Elongated Convective System (M $\beta$ ECS) (table 3). Finally, a last classification is performed by associating the DCS with the synoptic tropical storm recorded in the IBTrACS database. As introduced in (Hennon et al., 2011), a system located within a 1000 km radius of a cyclone is flagged according the storm type and the SSHS category (table 3).

The Analyses of DCS database can be conducted regions per regions. However, to focus on the whole tropical belt, we restrict the spatial coverage for each region to prevent double counting a same DCS identified in two adjacent geostationary platforms. Table 4 defines the spatial coverages to apply on each region of interest according to the configuration of the GEOring, which evolves along the period. A quality control indicator is associated to each identified DCS to indicate whether the cloud system has been impacted by interruptions/restarts, image edges, or missing images. Hence, 0.35 % of the total DCS population is found to be impacted by recovery and interruption of the tracking algorithm, with a maximum for the American (1.76 %) and Eastern Pacific regions (1.47 %), explained by the rapid scan operation modes of GOES-13 and GOES-15.

By filtering DCS which do not pass this quality control, a total of around  $15 \times 10^6$  DCS has been identified and tracked by TOOCAN from 2012 to 2020 over the entire tropical belt ( $30^\circ$  S- $30^\circ$  N),  $\sim 9 \times 10^6$  over the oceans,  $\sim 4.1 \times 10^6$  over the continents and  $1.7 \times 10^6$  over coastal regions. Oceanic convective systems are described by a slightly longer average lifetime duration

(6.25 h) than continental systems (6 h). Oceanic systems can last up to 102h, while the continental ones reach a maximum of 43.5 h. A large majority of convective systems are characterized by a maximum area between  $1 \times 10^3$  and  $2 \times 10^5$  km<sup>2</sup>, but some of them can reach a maximum extent up to  $2.3 \times 10^6$  km<sup>2</sup> over the ocean and  $1.3 \times 10^6$  km<sup>2</sup> over continents.

DCS Classifications	Definition	Contribution to population (%)	Contribution to cold cloudiness (%)	references
<b>Class 1</b>	- DCS with a lifetime duration < 5h	36.7	5.5	Roca et al. (2017)
<b>Class 2a</b>	DCS with a lifetime duration > 5h and describing only one maximum of their surface along their life cycle	52.8	84	
<b>Class2b</b>	DCS with a lifetime duration > 5h and describing several maximum of their surface along their life cycle	10.5	10.5	
<b>MCC</b>	- Cold cloud region $\leq 52^\circ$ with area $\geq 50\,000$ km <sup>2</sup> - Size definition met for $\geq 6$ h - Eccentricity > 0.7 at time of maximum extent	0.08	3.3	Jrak et al. (2003)
<b>PECS</b>	- Cold cloud region $\leq 52^\circ$ with area $\geq 50\,000$ km <sup>2</sup> - Size definition met for $\geq 6$ h - $0.2 \leq$ Eccentricity < 0.7 at time of maximum extent	0.08	3	
<b>M<math>\beta</math>CCS</b>	- Cold cloud region $\leq 52^\circ$ with area $\geq 50\,000$ km <sup>2</sup> - Size definition met for $\geq 6$ h - Eccentricity > 0.7 at time of maximum extent	0.3	3.9	
<b>M<math>\beta</math>ECS</b>	- Cold cloud region $\leq 52^\circ$ with area $\geq 50\,000$ km <sup>2</sup> - Size definition met for $\geq 6$ h - $0.2 \leq$ Eccentricity < 0.7 at time of maximum extent	0.41	5.36	
<b>MCC</b>	- Cold cloud shield $\leq 32^\circ$ with area $\geq 100\,000$ km <sup>2</sup> - Interior Cold cloud region $\leq 52^\circ$ with area $\geq 50\,000$ km <sup>2</sup> - Size definition met for $\geq 6$ h - Eccentricity > 0.7 at time of maximum extent	0.04	2.31	
<b>Mixture</b>		0.03	0.03	Maaddox (1980)
<b>Not reported</b>		0.77	1.2	
<b>subtropical</b>		0.27	0.34	
<b>Extratropical</b>		0.01	0.01	
<b>Disturbance</b>		0.01	0.01	
<b>Tropical</b>	- DCS located at a maximum distance of 1000km from a tropical storm identified and saved into the IBTrACS database	3	5	
<b>SSHS category 1</b>		0.41	0.82	
<b>SSHS category 2</b>		0.2	0.41	
<b>SSHS category 3</b>		0.22	0.46	
<b>SSHS category 4</b>		0.2	0.46	
<b>SSHS category 5</b>		0.01	0.04	

450 **Table 3** DCS classifications and physical characteristics used in the TOOCAN database

Regarding the system classifications, systems belonging to Class 1 contribute to 36.7 % of the total population but only 5.5 % of the cold cloudiness area (table 3). Class 2a convective systems contribute to 52.8 % of the total population and 84% of the cold cloudiness area, consistent with the results obtained in Roca et al. (2017a). Convective systems classified as MCC according to the definition given by Jirak et al. (2003), represent only 0.08 % of the total population but contribute to 3.3 % of the cold cloudiness area. Finally, a total of 156594 DCS are included within a 1000 km radius of a tropical cyclone (1 % of the total population), and only 2081 of them are associated to a category 5 cyclone (SSHS).

Region		Period					
		01/2012 05/2015	06/2015 12/2016	01/2017 12/2017	01/2018 11/2018	12/2018 12/2019	01/2020 12/2020
Effective spatial coverage	AFRICA	37,5°W-37,5°E 30°S-30°N	37,5°W-37,5°E 30°S-30°N	37,5°W-37,5°E 30°S-30°N	37,5°W-37,5°E 30°S-30°N	37,5°W-37,5°E 30°S-30°N	37,5°W-37,5°E 30°S-30°N
	INDIA	37,5°E-101,5°E 30°S-30°N	37,5°E-101,5°E 30°S-30°N	37,5°E-91,5°E 30°S-30°N	37,5°E-91,5°E 30°S-30°N	37,5°E-91,5°E 30°S-30°N	37,5°E-91,5°E 30°S-30°N
	WESTERNPACIFIC	101,5°E-184,5°E 30°S-30°N	101,5°E-184,5°E 30°S-30°N	91,5°E-184,5°E 30°S-30°N	91,5°E-184,5°E 30°S-30°N	91,5°E-184,5°E 30°S-30°N	91,5°E-184,5°E 30°S-30°N
	EASTERNPACIFIC	184,5°E-251,5°E 30°S-30°N	184,5°E-251,5°E 30°S-30°N	184,5°E-251,5°E 30°S-30°N	184,5°E-240,5°E 30°S-30°N	184,5°E-240,5°E 30°S-30°N	184,5°E-240,5°E 30°S-30°N
	AMERICA	108,5°W-37,5°W 30°S-30°N	108,5°W-37,5°W 30°S-30°N	108,5°W-37,5°W 30°S-30°N	119,5°W-37,5°W 30°S-30°N	119,5°W-37,5°W 30°S-30°N	119,5°W-37,5°W 30°S-30°N

**Table 4** Effective spatial coverage to be applied to each region and for the periods corresponding to specific GEOing configurations for a tropical belt analysis

#### 4.2.1 An illustration of the TOOCAN database

The annual climatology of the occurrence and morphological characteristics of deep convective systems is shown Fig. 9 in a phase diagram using lifetime duration and maximum extent as coordinates. Here, DCS within a 1000 km radius of a tropical cyclone have been removed from this analysis.

The distribution is described by systems lasting few hours and reaching around 1000km<sup>2</sup> to systems lasting several days and reaching up to few millions km<sup>2</sup> (Figure 9a). While a strong relationship is observed between lifetime duration and the maximum extent at first order, it is to also be noticed that a same lifetime duration can be associated to a large spread of maximum extent. Fig. 9b shows also that the larger the cloud shield, the colder the temperatures at the top of the cloud and therefore the deeper the cloud. Similar to Roca et al. (2024), both land and ocean distributions are described by a “V” pattern with two branches associated with the warmer systems. The shape of the cloud shield of the system is shown in Fig. 9c, with the distribution of the eccentricity of the cloud shield at the time of maximum extent along the life cycle. The eccentricity is defined by ratio of semi-minor axis to semi-major axis of the equivalent ellipse. While the largest and coldest deep convective systems are characterized by circularity of their cold cloud shields (eccentricity > 0.7), the warmer DCS located in the two branches of the “V” pattern are more characterized by linear shapes of their cold cloud shields (eccentricity < 0.5). The

distribution of the average speed according to maximum extent and lifetime duration is shown Fig. 9d. The fastest systems are found in the upper part of the distribution, while the slowest are found in its lower part. These features are more pronounced over the ocean compared to land.

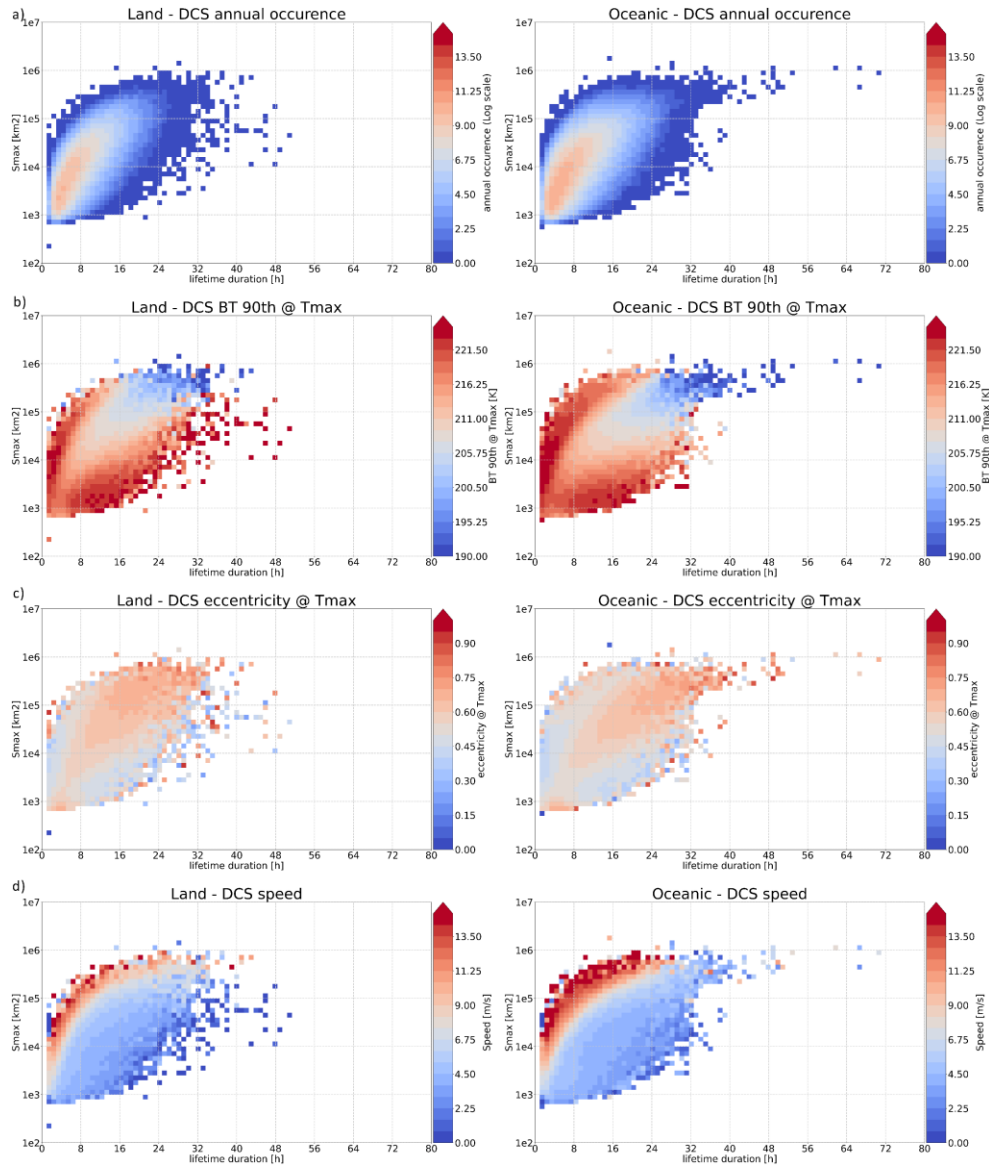


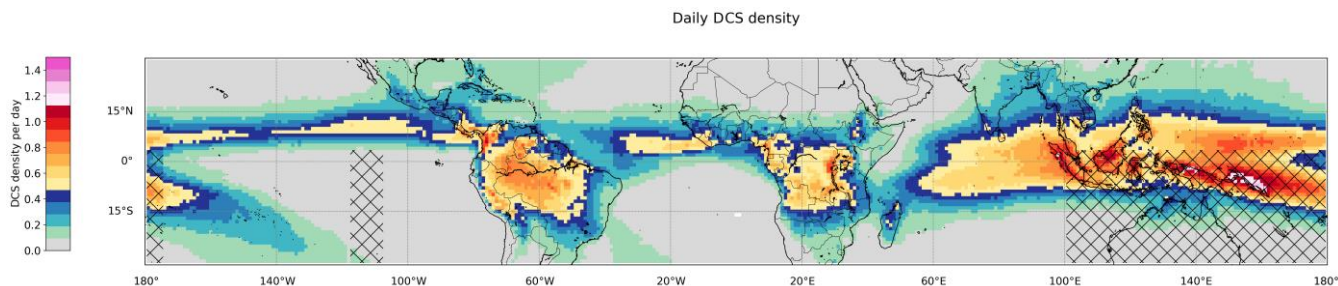
**Figure 9** (a) annual occurrence of the deep convective systems for continental (left) and the oceanic region; (b) 90<sup>th</sup> percentile of the cluster brightness temperature at the time of maximum extent; (c) eccentricity of the cluster at the time of maximum extent; (d) movement speed of the deep convective system

### 4.3 CACATOES dataset

The CACATOES database is a level-3 product derived from the TOOCAN database allowing a Eulerian view of the deep convective systems properties from a grid box perspective. The method was introduced and used in several studies (Roca and Fiolleau 2020, Berthet et al., 2017, Roca et al., 2014) and makes it easier the joint analysis with auxiliary data gridded on the same daily  $1^\circ \times 1^\circ$  grid box. The integrated morphological parameters of each DCS is gridded into a  $1^\circ \times 1^\circ$  daily grid (Table C1). For that, the full resolution pixels composing the convective systems identified within the TOOCAN segmented images are projected into each daily  $1^\circ \times 1^\circ$  grid box. The cold cloudiness fraction of each DCS which overpasses a given daily grid box is computed, and their morphological properties are assigned to that particular grid box. If cold cloud shield of a given DCS overpasses more than one daily grid box, the cold cloudiness of this given DCS is hence distributed onto each of the associated daily grid boxes. Similarly, when a system is lasting more than a day, the associated cold cloudiness is distributed over all the relevant days. Owing to the DCS propagation, cold cloud surfaces and lifetime durations, several systems can overpass a same  $1^\circ \times 1^\circ$  grid box during one day. In that case, they contribute all together to the total cold cloudiness of this given grid box. It has been defined that a maximum of 25 individual systems can overpass each grid box in a day. Within a given daily  $1^\circ \times 1^\circ$  grid box, the DCS morphological properties are finally sorted according to their cold cloudiness occupation, so that the most representative DCS can be easily identified. Roca and Fiolleau (2020) have shown that a couple of DCS impacts significantly each daily  $1^\circ \times 1^\circ$  grid box, while most of the other systems have very small contributions to the cold cloudiness. The statistical analysis of the DCS morphological parameters requires special cares when considered in a Eulerian framework. For instance, a DCS with a long lifetime duration may overpass only a few moments and a small footprint of a daily  $1^\circ \times 1^\circ$  grid box skewing the statistical results. Therefore, the average of a given morphological parameter over a region and time period has to be weighted using the actual cloud occupation of each system within each grid box. Similarly, the computation of the DCS population over a region and time period has to be considered with caution and can be computed by the sum of all the systems cold cloud fractions overpassing the daily grid boxes.

#### 4.3.1 An illustration of the CACATOES database

Figure 10 shows the daily  $1^\circ \times 1^\circ$  spatial distribution of the DCS density calculated from January 2012 to December 2020 over the entire tropical belt. The hatched areas indicate that the southern part of the Western and a southern band between  $118^\circ$  W and  $108^\circ$  W of the Eastern Pacific regions have been affected by missing data respectively from January 2012 to May 2015 and January 2012 to November 2017 respectively. The DCS density of these two specific regions have then been computed with a lower number of days involved. This may impact the patterns of DCS density, and therefore we would like to emphasize to future users that the analysis should be carried out with caution. Also, note that the map was built considering only days not impacted by any tracking interruptions over the any part of the tropical region and corresponding to 61.5 % of the total number of days over the entire 2012-2020 period. This number is mainly explained by the interruption of the southern scans of GOES-13 and GOES-15 due to Rapid Scan Operations



515 **Figure 10** Map of the deep convective systems density per day for a  $1^\circ \times 1^\circ$  grid box from January 2012 to December 2020. The hatched areas indicate missing data over the southern part of the Western and Eastern Pacific regions from January 2012 to May 2015 and from January 2012 to November 2017 respectively.

The geographical distribution of DCS density per day is consistent with previous DCS climatology based on other definitions, algorithms and satellite observations, either from local or global studies (Mohr and Zipser 1996, Liu et al. 2008, Feng et al. 2021, Huang et al. 2018). A zonal and homogeneous structure occurs over the Atlantic Ocean extending from the Guinean coast to  $40^\circ\text{W}$  (Machado et al., 1992). The Indian Ocean shows a large and zonally structured region, corresponding to the ITCZ (Roca and Ramanathan, 2000). On the continent, the West African deep convective systems extend no further north than  $17^\circ\text{N}$ , and the Indian Ocean convective systems extend to the foot of the Himalayas. DCS are also numerous over the western half of the maritime continent (Williams and Houze, 1987) with similar occurrence to that of Southeast Asia and the Philippines. The eastern Pacific ITCZ is also characterized by a large occurrence of DCS.

## 5 Data Format

### 5.1 TOOCAN Data format

The TOOCAN database is composed by two types of files. Regional TOOCAN segmented images at a  $0.04^\circ$  spatial resolution are produced every 30-minutes in a NetCDF-4 format with metadata following the Climate and Forecast (CF) Convention version 1.6 and Attribute Convention for Dataset Discovery (ACDD) version 1.3. The TOOCAN segmented images files contain the following information:

- **DCS\_number**: labelled pixels of the convective systems identified by the TOOCAN algorithm.
- **latitude**: the latitude values of the grid, in degrees, ranging between ( $-40^\circ\text{N}, 40^\circ\text{N}$ )
- **longitude**: the longitude values of the grid, in degrees
- 535 - **time**: the starting time scan of the image in seconds, since 1<sup>st</sup> January 1970
- **scantime**: time in seconds since 1<sup>st</sup> January 1970 at which each line of the TOOCAN segmented image is scanned by the geostationary platform.



Regional and monthly tracking files are produced in a NETCDF-4 format with metadata following the Climate and Forecast (CF) Convention version 1.6 and Attribute Convention for Dataset Discovery (ACDD) version 1.3 to document the DCS  
540 integrated morphological parameters as well as the DCS parameters at each 30minute-step of their life cycles. Note that similar regional and monthly tracking files have also been produced in an ASCII format, in order to ensure a continuity with previous versions of TOOCAN databases

Only the deep convective systems which initiate in a given month are stored in the corresponding monthly tracking file. If a DCS is initiated in a given month, but its dissipation extends beyond the end of that same month, the complete life cycle of  
545 this DCS is recorded in the file for the month corresponding to its birth. Each DCS is described by a unique label, and the link can be easily established between a given DCS described in a monthly tracking file and the pixels constituting this given DCS within the TOOCAN segmented images.

## 5.2 CACATOES Data Format

The 1°x1°-1day CACATOES tropical monthly files, describing the characteristics of DCS overpassing the daily 1° x1° lon/lat  
550 grid boxes, are also produced in a NetCDF-4 format with metadata following the Climate and Forecast (CF) Convention version 1.6 and Attribute Convention for Dataset Discovery (ACDD) version 1.3

## 5.3 Data availability

The TOOCAN database is available over the 2012-2020 period for each region of interest with a 40° S-40° N latitudinal  
555 coverage (Eastern-Pacific, America, Africa, India, Western-Pacific) in the following link: <https://doi.org/10.14768/1be7fd53-8b81-416e-90d5-002b36b30cf8> (Fiolleau and Roca, 2023). The CACATOES database, derived from the TOOCAN dataset, is available for the 2012-2020 period over the whole tropical belt [30°S-30°N] in the following link: <https://doi.org/10.14768/98569eea-d056-412d-9f52-73ea07b9cdca> (Fiolleau and Roca, 2023). The 2012-2020 homogenized infrared geostationary level-1C dataset described in this paper, and on which has been applied the TOOCAN algorithm can be  
560 accessed via the repository under the following data DOI: <https://doi.org/10.14768/93f138f5-a553-4691-96ed-952fd32d2fc3> (Fiolleau and Roca, 2023). The DOI landing pages provide the up-to-date information on how to access the database as well as a number of useful references for users.

## 6 Conclusions and outlook

A unique database of the deep convective systems and their morphological characteristics covering the 2012-2020 period over  
565 the intertropical belt has been introduced. The DCS morphology is obtained thanks to the TOOCAN tracking algorithm applied on a homogenized GEOring infrared archive. The homogenized GEOring database has been built from level-1 data of a fleet

of geostationary platforms originating from various sources. The temporal and spatial resolution of this GEOring archive is respectively 30 minutes and 0.04°. The GEOring dataset has been further inter-calibrated, spectrally adjusted, and limb darkening corrected, specifically for the high cold cloud shield, onto a common reference, the IR channel of the ScaRaB radiometer on-board Megha-Tropiques following the methodology introduced in Fiolleau et al. (2020). The global homogeneity of the IR GEOring dataset is then characterized by residual error of 1.33 K. Over the 9-year period, the configuration of the geostationary fleet nevertheless drastically changes. In June 2015, MTSAT is then replaced by HIMAWARI-8 over the Western Pacific Ocean. In January 2017, the end of operation of METEOSAT-7 corresponds to the arrival of MSG-1. Finally GOES-16 and GOES-17 have become operational respectively in December 2017 over the American and in January 2020 for the East Pacific Ocean.

An assessment of the sensitivity of the DCS identified by TOOCAN to the radiometric errors of the homogenized GEOring has been carried out. This analysis has shown a very small impact of a 1.5 K residual error on the DCS occurrences whatever their lifetime durations. Similarly, we have evaluated the impact of consecutive missing images on the quality of the DCS tracking. By filling the missing data periods by the available IR data just before and after the missing data gap, we have shown that up to 3 h period of consecutive missing images, the impact is relatively small on the DCS occurrences. Hence, the occurrence of systems lasting more than 10h is skewed by 20 % for a 3 h period of consecutive missing images. Beyond 3 h of consecutive missing images, the impact on the DCS segmentation is too high, and the tracking process has to be stopped.

The TOOCAN algorithm has then been processed on the homogenized GEOring IR data over the 2012-2020 period and on the latitude band 40° S-40° N. The resulting database gives an access to the integrated morphological parameters of each DCS (Location and time of initiation and dissipation, lifetime duration, propagated distance, cold cloud maximum extent...), as well as the evolution of the morphological properties along the DCS life cycles. The DCS located near a cyclone identified in the IBTrACS database (Knapp et al., 2010) have been flagged. A total of  $15 \times 10^6$  DCS have been detected and tracked by TOOCAN over the tropical regions and the 9-year period. The analysis of DCS database over the tropical oceans and continents shows the large variety of DCS characteristics and organization encountered. DCS can last few hours up to several days, and are distributed by cloud surfaces from 1000 km<sup>2</sup> to few millions of km<sup>2</sup>. Oceanic DCS are described by a longer lifetime duration and larger cold cloud surfaces. Over the both regions, while a strong relationship is observed between lifetime duration and Maximum surface extent in a first order, we can also notice a large spectrum of maximum extent for a given lifetime duration. The 2D spatial distribution of DCS density over the Tropics is also in line with previous DCS climatology produced from other formulation of tracking algorithms and geostationary IR dataset (Feng et al. 2021, Huang et al. 2018, Rajagopal et al. 2023).

595

## Appendix A

An example of a header of the netCDF-4 file for the TOOCAN monthly tracking file.

dimensions:

600 DCS = 40915 ;

time = UNLIMITED ; // (1523 currently)

variables:

int time(time) ;

time:units = "seconds since 1970-01-01" ;

605 time:long\_name = "time" ;

int DCS(DCS) ;

DCS:units = "none" ;

DCS:long\_name = "Label of the Deep Convective Systems" ;

int INT\_DCSnumber(DCS) ;

610 INT\_DCSnumber:\_FillValue = -999 ;

INT\_DCSnumber:units = "" ;

INT\_DCSnumber:long\_name = "Label of the DCS in the TOOCAN segmented images" ;

int INT\_DCS\_qualitycontrol(DCS) ;

INT\_DCS\_qualitycontrol:\_FillValue = -999 ;

615 INT\_DCS\_qualitycontrol:units = "" ;

INT\_DCS\_qualitycontrol:long\_name = "Quality control on the DCS initiation/dissipation..." ;

int INT\_classif(DCS) ;

INT\_classif:\_FillValue = -999 ;

INT\_classif:units = "" ;

620 INT\_classif:long\_name = "Classification of the DCS according to Roca etal (2017)" ;

INT\_classif:flag\_values = 1, 2, 3 ;

INT\_classif:flag\_meanings = "DCS with a duration < 5hr, DCS with a duration  $\geq$  5hr and described by a single maximum of their cold surfaces along their life cycles, DCS with a duration  $\geq$  5hr and described by several maximums of their cold surfaces along their life cycles" ;

```

float INT_duration(DCS) ;

625     INT_duration:_FillValue = -999.f ;

        INT_duration:units = "hr" ;

        INT_duration:long_name = "DCS lifetime duration" ;

int INT.UTC_timeInit(DCS) ;

        INT.UTC_timeInit:_FillValue = -999 ;

630     INT.UTC_timeInit:units = "seconds since 1st January 1970" ;

        INT.UTC_timeInit:long_name = "Universal Time of the DCS initiation " ;

int INT.localtime_Init(DCS) ;

        INT.localtime_Init:_FillValue = -999 ;

        INT.localtime_Init:units = "seconds since 1st January 1970" ;

635     INT.localtime_Init:long_name = "Local time of the DCS initiation initiation" ;

float INT_lonInit(DCS) ;

        INT_lonInit:_FillValue = -999.f ;

        INT_lonInit:units = "degrees" ;

        INT_lonInit:long_name = "Longitude of the DCS center of mass at its initiation" ;

640     float INT_latInit(DCS) ;

        INT_latInit:_FillValue = -999.f ;

        INT_latInit:units = "degrees" ;

        INT_latInit:long_name = "Latitude of the DCS center of mass at its initiation" ;

int INT.UTC_timeEnd(DCS) ;

645     INT.UTC_timeEnd:_FillValue = -999 ;

        INT.UTC_timeEnd:units = "seconds since 1st January 1970" ;

        INT.UTC_timeEnd:long_name = "Coordinated Universal Time of the DCS dissipation" ;

int INT.localtime_End(DCS) ;

        INT.localtime_End:_FillValue = -999 ;

650     INT.localtime_End:units = "seconds since 1st January 1970" ;

```

```
    INT_localtime_End:long_name = "Local time of the DCS dissipation" ;

float INT_lonEnd(DCS) ;

    INT_lonEnd:_FillValue = -999.f ;

    INT_lonEnd:units = "degrees" ;

655    INT_lonEnd:long_name = "Longitude of the DCS center of mass at its dissipation" ;

float INT_latEnd(DCS) ;

    INT_latEnd:_FillValue = -999.f ;

    INT_latEnd:units = "degrees" ;

    INT_latEnd:long_name = "Latitude of the DCS center of mass at its dissipation" ;

660 float INT_velocityAvg(DCS) ;

    INT_velocityAvg:_FillValue = -999.f ;

    INT_velocityAvg:units = "m/s" ;

    INT_velocityAvg:long_name = "Average velocity of the DCS from its initiation to its dissipation" ;

float INT_distance(DCS) ;

665    INT_distance:_FillValue = -999.f ;

    INT_distance:units = "km" ;

    INT_distance:long_name = "DCS propagated distance" ;

float INT_lonmin(DCS) ;

    INT_lonmin:_FillValue = -999.f ;

670    INT_lonmin:units = "degrees" ;

    INT_lonmin:long_name = "Minimum longitude of the DCS along its life cycle" ;

float INT_lonmax(DCS) ;

    INT_lonmax:_FillValue = -999.f ;

    INT_lonmax:units = "degrees" ;

675    INT_lonmax:long_name = "Maximum latitude of the DCS along its life cycle" ;

float INT_latmin(DCS) ;

    INT_latmin:_FillValue = -999.f ;
```

```

INT_latmin:units = "degrees" ;

INT_latmin:long_name = "Minimum longitude of the DCS along its life cycle" ;

680 float INT_latmax(DCS) ;

INT_latmax:_FillValue = -999.f ;

INT_latmax:units = "degrees" ;

INT_latmax:long_name = "Maximum latitude of the DCS along its life cycle" ;

float INT_tbmin(DCS) ;

685 INT_tbmin:_FillValue = -999.f ;

INT_tbmin:units = "K" ;

INT_tbmin:long_name = "Minimum brightness temperature of the DCS along its life cycle" ;

int INT_surfmaxPix_235K(DCS) ;

INT_surfmaxPix_235K:_FillValue = -999 ;

690 INT_surfmaxPix_235K:units = "number of pixels" ;

INT_surfmaxPix_235K:long_name = "Maximum cold cloud surface at 235K reached by the DCS along its life cycle" ;

float INT_surfmaxkm2_235K(DCS) ;

INT_surfmaxkm2_235K:_FillValue = -999.f ;

INT_surfmaxkm2_235K:units = "km2" ;

695 INT_surfmaxkm2_235K:long_name = "Maximum cold cloud surface at 235K reached by the DCS along its life cycle " ;

float INT_surfmaxkm2_220K(DCS) ;

INT_surfmaxkm2_220K:_FillValue = -999.f ;

INT_surfmaxkm2_220K:units = "km2km2" ;

INT_surfmaxkm2_220K:long_name = "Maximum cold cloud surface at 220K reached by the DCS along its life cycle" ;

700 float INT_surfmaxkm2_210K(DCS) ;

INT_surfmaxkm2_210K:_FillValue = -999.f ;

INT_surfmaxkm2_210K:units = "km2" ;

INT_surfmaxkm2_210K:long_name = "Maximum cold cloud surface at 210K reached by the DCS along its life cycle" ;

float INT_surfmaxkm2_200K(DCS) ;

```

```

705     INT_surfmaxkm2_200K:_FillValue = -999.f ;

        INT_surfmaxkm2_200K:units = "km2" ;

        INT_surfmaxkm2_200K:long_name = "Maximum cold cloud surface at 200K reached by the DCS along its life cycle" ;

float INT_surfcumkm2_235K(DCS) ;

        INT_surfcumkm2_235K:_FillValue = -999.f ;

710     INT_surfcumkm2_235K:units = "km2" ;

        INT_surfcumkm2_235K:long_name = "Cumulated cold cloud surface at 235K along the DCS life cycle" ;

int INT_classif_JIRAK(DCS) ;

        INT_classif_JIRAK:_FillValue = -999 ;

        INT_classif_JIRAK:units = "none" ;

715     INT_classif_JIRAK:long_name = "DCS classification according to the JIRAK definition (Jirak etal (2003))" ;

        INT_classif_JIRAK:flag_values = 0, 1, 2, 3, 4 ;

        INT_classif_JIRAK:flag_meanings = "no classification,MCC,PECS,MBCC,MBECC" ;

int INT_classif_MADDOX(DCS) ;

        INT_classif_MADDOX:_FillValue = -999 ;

720     INT_classif_MADDOX:units = "none" ;

        INT_classif_MADDOX:long_name = "DCS classification according to the MADDOX definition Maddox (1980)" ;

        INT_classif_MADDOX:flag_values = 0, 1, 2, 3, 4, 5, 6, 7, 8, 9, 10, 11, 12, 13, 14, 15 ;

        INT_classif_MADDOX:flag_meanings = "no matching with TS, Mixture, Not reported, disturbance, subtropical storm, extratropical storm, tropical
storm, cyclone SSHS category 1, cyclone SSHS category 2, cyclone SSHS category 3, cyclone SSHS category 4, cyclone SSHS category 5" ;

725     int INT_TS_number_IBTRACS(DCS) ;

        INT_TS_number_IBTRACS:_FillValue = -999 ;

        INT_TS_number_IBTRACS:units = "none" ;

        INT_TS_number_IBTRACS:long_name = "number of the Tropical Storm in the IBTRACS database associated with the DCS within a 1000km
radius" ;

730     int INT_TS_nature_IBTRACS(DCS) ;

        INT_TS_nature_IBTRACS:_FillValue = -999 ;

        INT_TS_nature_IBTRACS:units = "none" ;

```

```

INT_TS_nature_IBTRACS:long_name = "nature of the Tropical Storm in the IBTRACS database" ;

float INT_TS_mindistance_IBTRACS(DCS) ;

735 INT_TS_mindistance_IBTRACS:_FillValue = -999.f ;

INT_TS_mindistance_IBTRACS:units = "km2" ;

INT_TS_mindistance_IBTRACS:long_name = "Distance of the DCS to the Tropical Storm (maximum distnace: 1000km)" ;

int QCgeo_IRimage(time) ;

QCgeo_IRimage:_FillValue = -999 ;

740 QCgeo_IRimage:units = "nodimension" ;

QCgeo_IRimage:long_name = "Quality control on the GEO IR data" ;

QCgeo_IRimage:flag_values = 0, 1, 2 ;

QCgeo_IRimage:flag_meanings = "Missing GEO IR data, The Full GEO IR data OK, The Only North scan of GEO IR data OK" ;

float LC_tbmin(DCS, time) ;

745 LC_tbmin:_FillValue = -999.f ;

LC_tbmin:units = "K" ;

LC_tbmin:long_name = "Minimum brightness temperature" ;

float LC_tbavg_235K(DCS, time) ;

LC_tbavg_235K:_FillValue = -999.f ;

750 LC_tbavg_235K:units = "K" ;

LC_tbavg_235K:long_name = "Average brightness temperature at 235K" ;

float LC_tbavg_208K(DCS, time) ;

LC_tbavg_208K:_FillValue = -999.f ;

LC_tbavg_208K:units = "K" ;

755 LC_tbavg_208K:long_name = "Average brightness temperature at 208K" ;

float LC_tbavg_200K(DCS, time) ;

LC_tbavg_200K:_FillValue = -999.f ;

LC_tbavg_200K:units = "K" ;

LC_tbavg_200K:long_name = "Average brightness temperature at 200K" ;

```



```

760 float LC_tb90th(DCS, time) ;

    LC_tb90th:_FillValue = -999.f ;

    LC_tb90th:units = "K" ;

    LC_tb90th:long_name = "Tb 90th percentile" ;

int LC.UTC_time(DCS, time) ;

765 LC.UTC_time:_FillValue = -999 ;

    LC.UTC_time:units = "seconds since 1st January 1970" ;

    LC.UTC_time:long_name = "Coordinated Universal Time of the DCS " ;

int LC.localtime(DCS, time) ;

    LC.localtime:_FillValue = -999 ;

770 LC.localtime:units = "seconds since 1st January 1970" ;

    LC.localtime:long_name = "Local Time of the DCS " ;

float LC_lon(DCS, time) ;

    LC_lon:_FillValue = -999.f ;

    LC_lon:units = "degrees" ;

775 LC_lon:long_name = "longitude of the DCS center of mass" ;

float LC_lat(DCS, time) ;

    LC_lat:_FillValue = -999.f ;

    LC_lat:units = "degrees" ;

    LC_lat:long_name = "latitude of the DCS center of mass" ;

780 int LC_x(DCS, time) ;

    LC_x:_FillValue = -999 ;

    LC_x:units = "pixels" ;

    LC_x:long_name = "Column of the DCS center of mass" ;

int LC_y(DCS, time) ;

785 LC_y:_FillValue = -999 ;

    LC_y:standard_name = "pixels" ;

```

```
LC_y:long_name = "Line of the DCS center of mass" ;

float LC_velocity(DCS, time) ;

LC_velocity:_FillValue = -999.f ;

790 LC_velocity:units = "m/s" ;

LC_velocity:long_name = "instantaneous velocity" ;

float LC_semiminor_235K(DCS, time) ;

LC_semiminor_235K:_FillValue = -999.f ;

LC_semiminor_235K:units = "km" ;

795 LC_semiminor_235K:long_name = "Semi-minor axis of the equivalent ellipse at a 235K threshold" ;

float LC_semimajor_235K(DCS, time) ;

LC_semimajor_235K:_FillValue = -999.f ;

LC_semimajor_235K:units = "km" ;

LC_semimajor_235K:long_name = "Semi-major axis of the equivalent ellipse at a 235K threshold" ;

800 float LC_ecc_235K(DCS, time) ;

LC_ecc_235K:_FillValue = -999.f ;

LC_ecc_235K:units = "semiminor/semimajor" ;

LC_ecc_235K:long_name = "Eccentricity of the equivalent ellipse at a 235K threshold" ;

float LC_orientation_235K(DCS, time) ;

805 LC_orientation_235K:_FillValue = -999.f ;

LC_orientation_235K:units = "degrees" ;

LC_orientation_235K:long_name = "orientation of the equivalent ellipse at a 235K threshold" ;

float LC_semiminor_220K(DCS, time) ;

LC_semiminor_220K:_FillValue = -999.f ;

810 LC_semiminor_220K:units = "km" ;

LC_semiminor_220K:long_name = "Semi-minor axis of the equivalent ellipse at a 220K threshold" ;

float LC_semimajor_220K(DCS, time) ;

LC_semimajor_220K:_FillValue = -999.f ;
```

```

LC_semimajor_220K:units = "km" ;
815 LC_semimajor_220K:long_name = "Semi-major axis of the equivalent ellipse at a 220K threshold" ;
float LC_ecc_220K(DCS, time) ;
LC_ecc_220K:_FillValue = -999.f ;
LC_ecc_220K:units = "semiminor/semimajor" ;
LC_ecc_220K:long_name = "Eccentricity of the equivalent ellipse at a 220K threshold" ;
820 float LC_orientation_220K(DCS, time) ;
LC_orientation_220K:_FillValue = -999.f ;
LC_orientation_220K:units = "degrees" ;
LC_orientation_220K:long_name = "orientation of the equivalent ellipse at a 220K threshold" ;
int LC_surfPix_235K(DCS, time) ;
825 LC_surfPix_235K:_FillValue = -999 ;
LC_surfPix_235K:units = "number of pixels" ;
LC_surfPix_235K:long_name = "Cold cloud surface in number of pixels of the convective cluster for a 235K threshold" ;
int LC_surfPix_210K(DCS, time) ;
LC_surfPix_210K:_FillValue = -999 ;
830 LC_surfPix_210K:units = "number of pixels" ;
LC_surfPix_210K:long_name = "Cold cloud surface in number of pixels of the convective cluster for a 210K threshold" ;
float LC_surfkm2_235K(DCS, time) ;
LC_surfkm2_235K:_FillValue = -999.f ;
LC_surfkm2_235K:units = "km2" ;
835 LC_surfkm2_235K:long_name = "Cold cloud surface in km2 of the convective cluster for a 235K threshold" ;
float LC_surfkm2_220K(DCS, time) ;
LC_surfkm2_220K:_FillValue = -999.f ;
LC_surfkm2_220K:units = "km2" ;
LC_surfkm2_220K:long_name = "Cold cloud surface in km2 of the convective cluster for a 220K threshold" ;
840 float LC_surfkm2_210K(DCS, time) ;

```

```

LC_surfkm2_210K:_FillValue = -999.f ;

LC_surfkm2_210K:units = "km2" ;

LC_surfkm2_210K:long_name = "Cold cloud surface in km2 of the convective cluster for a 210K threshold" ;

float LC_surfkm2_200K(DCS, time) ;

845 LC_surfkm2_200K:_FillValue = -999.f ;

LC_surfkm2_200K:units = "km2" ;

LC_surfkm2_200K:long_name = "Cold cloud surface in km2 of the convective cluster for a 200K threshold" ;

// global attributes:

850 :title = "TOOCAN - Morphological characteristics of the Deep Convective Systems initiating between 01/01/2012 00:00 UTC and 01/31/2012 23:30
UTC" ;

:creator_name = "Thomas Fiolleau" ;

:contributor_name = "Remy Roca" ;

:contact = "thomas.fiolleau@cnr.fr" ;

855 :institution = "CNRS/LEGOS/IPSL" ;

:conventions = "CF-1.6, ACDD-1.3" ;

:tracker = "TOOCAN" ;

:version = "2.08" ;

:Geostationary_platform = "MSG2" ;

860 :region = "AFRICA" ;

:region_longitude = "-55 - 55" ;

:region_latitude = "-40 - 40" ;

:temporal_resolution = "30 min" ;

:Spatial_resolution = "0.04 degree" ;

865 :time_coverage_start = "01/01/2012 00:00 UTC" ;

:time_coverage_End = "02/01/2012 17:00 UTC" ;

:DCS_occurrence = "40915" ;

```

## Appendix B

870 **Table B1.** Integrated morphological parameters of each identified deep convective systems documented in the TOOCAN netCDF-4 and ASCII monthly tracking files.

Integrated morphological parameters	Description	Units
DCS_number	Label of the DCS in the segmented images	/
INT_qltyDCS	Quality flag indicating if the DCS initiates or dissipates due to missing images	/
INT_classif	Classification of the DCS according to the Roca etal (2017) definition	/
INT_duration	Life time duration	hr
INT.UTC_timeInit	Universal Time of the DCS initiation	seconds since 01/01/1970
INT.localtime_Init	Local time of the DCS initiation	seconds since 01/01/1970
INT_lonInit	Longitude of the DCS center of mass at its initiation	degrees
INT_latInit	Latitude of the DCS center of mass at its initiation	degrees
INT.UTC_timeEnd	Coordinated Universal Time of the DCS dissipation	seconds since 01/01/1970
INT.localtime_End	Local time of the DCS dissipation	seconds since 01/01/1970
INT_lonEnd	Longitude of the DCS center of mass at its dissipation	degrees
INT_latEnd	Latitude of the DCS center of mass at its dissipation	degrees
INT_velocityAvg	Average velocity of the DCS from its initiation to its dissipation	m/s
INT_distance	Distance covered by the DCS	km
INT_lonmin	Minimum longitude of the DCS along its life cycle	degrees
INT_latmin	Minimum latitude of the DCS along its life cycle	degrees
INT_lonmax	Maximum longitude of the DCS along its life cycle	degrees
INT_latmax	Maximum latitude of the DCS along its life cycle	degrees
INT_TbMin	Minimum brightness temperature of the DCS along its life cycle	K
INT_surfmaxPix_235K	Maximum cloud surface reached by the DCS at 235K	number of pixels
INT_surfmaxkm2_235K	Maximum cloud surface reached by the DCS at 235K	km <sup>2</sup>
INT_surfmaxkm2_220K	Maximum cloud surface reached by the DCS at 220K	km <sup>2</sup>
INT_surfmaxkm2_210K	Maximum cloud surface reached by the DCS at 210K	km <sup>2</sup>
INT_surfmaxkm2_200K	Maximum cloud surface reached by the DCS at 200K	km <sup>2</sup>
INT_surfcumkm2_235K	DCS total cold cloudiness at 235K from its initiation to its dissipation	km <sup>2</sup>
INT_classif_JIRAK	DCS classification according to the Jirak etal (2003) definition	/
INT_classif_MADDOX	DCS classification according to the Maddox (1981) definition	/
INT_TSnumber_IBTRACS	number of the Tropical Storm in the IBTrACS file associated with the DCS in a 1000km radius	/
INT_TSnature_IBTRACS	nature of the Tropical Storm in the IBTrACS file	/

**Table B2.** morphological parameters described every 30 minutes along the life cycles of each deep convective systems documented in the TOOCAN netCDF-4 and ASCII monthly tracking files.

<b>morphological parameters along the DCS life cycles</b>	<b>Description</b>	<b>Units</b>
QCgeo_IRimage	Flag Indicating the IR missing image	
LC_tmin	Minimum brightness temperature	K
LC_tavg_235K	Average brightness temperature at 235K	K
LC_tavg_208K	Average brightness temperature at 208K	K
LC_tavg_200K	Average brightness temperature at 200K	K
LC_t_90th	90 <sup>th</sup> percentile of brightness temperature	K
LC.UTC_time	Coordinated Universal Time of the DCS	seconds since 01/01/1970
LC.localtime	Local time of the DCS	seconds since 01/01/1970
LC_lon	Longitude of the center of mass	degrees
LC_lat	Latitude of the center of mass	degrees
LC_x	Column of the center of mass in the image	Indices of the column
LC_y	Line of the center of mass in the image	Indices of the line
LC_velocity	Instantaneous velocity	m/s
LC_sminor_235K	Semi-minor axis of the ellipse at a 235K threshold	km
LC_smajor_235K	Semi-major axis of the ellipse at a 235K threshold	km
LC_ecc_235K	Eccentricity of the ellipse at a 235K threshold computed as $\frac{LC\_sminor\_235K}{LC\_smajor\_235K}$	/
LC_orientation_235K	Orientation of the ellipse at a 235K threshold	degrees
LC_sminor_220K	Semi-minor axis of the ellipse at a 220K threshold	km
LC_smajor_220K	Semi-major axis of the ellipse at a 220K threshold	km
LC_ecc_220K	Eccentricity of the ellipse for a 220K threshold computed as: $\frac{LC\_sminor\_220K}{LC\_smajor\_220K}$	/
LC_orientation_220K	Orientation of the ellipse at a 220K threshold	degrees
LC_surfPix_235K	Cold cloud surface of the convective cluster for a 235K threshold	number of pixels
LC_surfPix_210K	Cold cloud surface of the convective cluster for a 210K threshold	number of pixels
LC_surfkm2_235K	Cold cloud surface of the convective cluster for a 235k threshold	km <sup>2</sup>
LC_surfkm2_220K	Cold cloud surface of the convective cluster for a 220k threshold	km <sup>2</sup>
LC_surfkm2_210K	Cold cloud surface of the convective cluster for a 210k threshold	km <sup>2</sup>
LC_surfkm2_200K	Cold cloud surface of the convective cluster for a 200k threshold	km <sup>2</sup>

## Appendix C

880 **Table C1.** Morphological parameters of each DCS gridded into a  $1^\circ \times 1^\circ$  daily grid of the CACATOES netCDF-4 monthly files.

Variable	Description	Units
DAILY_DCS_Cloudcover	Daily cloud cover	%
QCgeo_numgeo	ID of the geostationary platform	/
QCgeo_nbMissingImages	Number of missing/corrupted geo images per day	/
QCgeo_GEOScanMode	Number of GEO images per day	/
QCtoocan_Interruption	Indication of a tracking interruption	/
QCtoocan_nbSegmentedImages	Number of TOOCAN segmented images	/
QCtoocan_trackingOK_allplatforms	Quality of the Tracking over the entire tropical belt	/
QCcacatoes_nbpixels	Number of GEO pixels within a $1^\circ/1\text{day}$ CACATOES gridpoint	/
QCcacatoes_SurfGridPoint	Cumulated GEO pixels surface into a CACATOES $1^\circ/1\text{day}$ gridpoint	/
INT_DCSnumber	Label of the DCS	/
QC_DCS	Confidence on the tracked DCS	/
INT_classif	DCSs classification according to Roca etal (2017) definition	/
INT_duration	Life time duration	h
INT_surfmaxkm2_235K	Maximum cold cloud surface reached by the DCS along its life cycle at 235K	km <sup>2</sup>
INT_surfmaxkm2_220K	Maximum cold cloud surface reached by the DCS along its life cycle at 220K	km <sup>2</sup>
INT_surfmaxkm2_210K	Maximum cold cloud surface reached by the DCS along its life cycle at 210K	km <sup>2</sup>
INT_surfmaxkm2_200K	Maximum cold cloud surface reached by the DCS along its life cycle at 200K	km <sup>2</sup>
INT_surfcumkm2_235K	Cumulated cold cloud surface of the DCS along its life cycle at 235K	km <sup>2</sup>
INT_Tmax	Time of maximum extent at 235K	%
INT_SurfDCS_220K_at_Tmax	DCS size at 220K at time of maximum extent	km <sup>2</sup>
INT_SurfDCS_210K_at_Tmax	DCS size at 210K at time of maximum extent	km <sup>2</sup>
INT_SurfDCS_200K_at_Tmax	DCS size at 200K at time of maximum extent	km <sup>2</sup>
INT_Tbavg235K_at_Tmax	average Tb lower than 235K at time of maximum extent	K
INT_Tbavg208K_at_Tmax	average Tb lower than 208K at time of maximum extent	K
INT_Tbavg200K_at_Tmax	average Tb lower than 200K at time of maximum extent	K
INT_Tb90th_at_Tmax	90th percentile of Tb at time of maximum extent	K
INT_Ecc220K_at_Tmax	eccentricity of the DCS at time of maximum extent for a 220K threshold computed as: $\frac{S_{minor\_220K}}{S_{major\_220K}}$	/
INT_Ecc235K_at_Tmax	eccentricity of the DCS at time of maximum extent for a 235K threshold computed as: $\frac{S_{minor\_235K}}{S_{major\_235K}}$	/
INT_orientation220K_at_Tmax	orientation of the DCS at time of maximum extent for a 220K threshold	degrees
INT_orientation235K_at_Tmax	orientation of the DCS at time of maximum extent for a 235K threshold	degrees
INT_Distance	Propagated distance covered by the DCS	km
INT_Tbmin	Minimum brightness temperature of the DCS along its life cycle	K
INT_SurfDCS_235K	DCS Integrated Surface at a 235K threshold within a CACATOES $1^\circ/1\text{day}$ grid point	km <sup>2</sup>
INT_SurfDCS_220K	DCS Integrated Surface at a 220K threshold within a CACATOES $1^\circ/1\text{day}$ grid point	km <sup>2</sup>
INT_SurfDCS_210K	DCS Integrated Surface at a 210K threshold within a CACATOES $1^\circ/1\text{day}$ grid point	km <sup>2</sup>

INT_SurfDCS_200K	DCS Integrated Surface at a 200K threshold within a CACATOES 1°/1day grid point	km <sup>2</sup>	
INT_GridFraction_235K	Fraction of the CACATOES 1°/1day grid point occupied by a DCS at a 235K threshold	%	
INT_GridFraction_220K	Fraction of the CACATOES 1°/1day grid point occupied by a DCS at a 220K threshold	%	
INT_GridFraction_210K	Fraction of the CACATOES 1°/1day grid point occupied by a DCS at a 210K threshold	%	
INT_GridFraction_200K	Fraction of the CACATOES 1°/1day grid point occupied by a DCS at a 200K threshold	%	
INT_gridtimeOccupation_start	start time of the grid point occupation by a DCS	hr since the start of the day	
INT_gridtimeOccupation_end	End time of the grid point occupation by a DCS	hr since the start of the day	
INT_Sfrac_235k	Fraction of the DCS within the CACATOES 1°/1day grid point at a 235K threshold	%	
INT_Sfrac_220K	Fraction of the DCS within the CACATOES 1°/1day grid point at a 220K threshold	%	
INT_Sfrac_210K	Fraction of the DCS within the CACATOES 1°/1day grid point at a 210K threshold	%	
INT_Sfrac_200K	Fraction of the DCS within the CACATOES 1°/1day grid point at a 220K threshold	%	
INT_TSnature_IBTRACS	nature of the Tropical Storm in the IBTrACS file	/	
INT_TSnumber_IBTRACS	number of the Tropical Storm in the IBTrACS file associated with the DCS in a 1000km radius	/	
INT_TSmindistance_IBTRACS	Distance of DCS to the IBTrACS Tropical Storm	Km	
INT_classif_JIRAK	DCS classification according to the Jirak etal (2003) definition	/	
INT_classif_MADDOX	DCS classification according to the Maddox (1980) definition	/	
INIT_Time	time of the DCS initiation	seconds	since 01/01/1970
INIT_Lon	Longitude of the DCS center of mass at its initiation	degrees	
INIT_Lat	Latitude of the DCS center of mass at its initiation	degrees	
END_Time	time of the DCS dissipation	seconds	since 01/01/1970
END_Lon	Longitude of the DCS center of mass at its dissipation	degrees	
END_Lat	Latitude of the DCS center of mass at its dissipation	degrees	

## Video supplement

885 Video S1 (<https://doi.org/10.5446/68200>, Fiolleau 2024) shows an animation of convective situation segmented by TOOCAN from HIMAWARI IR data over the Western Pacific region in October 2015.

## Author contributions

Thomas Fiolleau and Remy Roca initiated the work. Thomas Fiolleau and Remy Roca prepared some datasets. Thomas Fiolleau drafted the figures. All the authors contributed to the writing of the paper.



## Competing interests

890 The authors declare that they have no conflict of interest.

## Acknowledgements

This work has been supported by CNRS and CNES under the Megha-Tropiques program. We thank the ESPRI/IPSL team to providing computing and storage resources. We thank the French data center AERIS, and especially Sophie Cloché to help accessing the data (georing, ScaRaB). The authors thank also L. Gouttesoulard for his help handling the geostationary satellite data archive. The authors further acknowledge M. Dejus, project manager at CNES and his team for their help on the technical aspects of ScaRaB. They thank also Nuria Duran-Gomez and Rémi Jugier from MAGELLIUM for their contribution on the GEOring homogenization.

## References

- 900 Arkin, P. A.: The Relationship between Fractional Coverage of High Cloud and Rainfall Accumulations during GATE over the B-Scale Array, [https://doi.org/10.1175/1520-0493\(1979\)107<1382:TRBFCO>2.0.CO;2](https://doi.org/10.1175/1520-0493(1979)107<1382:TRBFCO>2.0.CO;2), 1979.
- Arnaud, Y., Desbois Michel, and Maizi Joël: Automatic Tracking and Characterization of African Convective Systems on Meteosat Pictures, *J. Appl. Meteor. Climatol*, 31, 443–453, [https://doi.org/https://doi.org/10.1175/1520-0450\(1992\)031<0443:ATACOA>2.0.CO;2](https://doi.org/https://doi.org/10.1175/1520-0450(1992)031<0443:ATACOA>2.0.CO;2), 1992.
- 905 Autones, F. and Moisselin, J.-M.: Algorithm Theoretical Basis Document for “Rapid Development Thunderstorms” (RDT-PGE11 v3.0), Scientific documentation of SAF/NWC, code SAF/NWC/CDOP2/MFT/SCI/ATBD/11, 2013.
- Bellerby, T., Hsu, K., and Sorooshian, S.: LMODEL: A Satellite Precipitation Methodology Using Cloud Development Modeling. Part I: Algorithm Construction and Calibration, *J Hydrometeorol*, 10, 1081–1095, <https://doi.org/10.1175/2009jhm1091.1>, 2009.
- 910 Berthet, S., Roca, R., Duvel, J. P., and Fiolleau, T.: Subseasonal variability of mesoscale convective systems over the tropical northeastern Pacific, *Quarterly Journal of the Royal Meteorological Society*, 143, <https://doi.org/10.1002/qj.2992>, 2017.
- Boer, E. R. and Ramanathan, V.: Lagrangian approach for deriving cloud characteristics from satellite observations and its implications to cloud parameterization, *Journal of Geophysical Research: Atmospheres*, 102, 21383–21399, <https://doi.org/10.1029/97JD00930>, 1997.

- 915 Bouniol, D., Roca, R., Fiolleau, T., and Poan, D. E.: Macrophysical, Microphysical, and Radiative Properties of Tropical Mesoscale Convective Systems over Their Life Cycle, *J Clim*, 29, 3353–3371, <https://doi.org/10.1175/jcli-d-15-0551.1>, 2016.
- Bouniol, D., Roca, R., Fiolleau, T., and Raberanto, P.: Life cycle–resolved observation of radiative properties of mesoscale convective systems, *J Appl Meteorol Climatol*, 60, 1091–1104, <https://doi.org/10.1175/JAMC-D-20-0244.1>, 2021.
- Carvalho, L. M. V. and Jones, C.: A Satellite Method to Identify Structural Properties of Mesoscale Convective Systems Based on the Maximum Spatial Correlation Tracking Technique (MASCOTTE), *Journal of Applied Meteorology*, 40, 1683–1701, [https://doi.org/10.1175/1520-0450\(2001\)040<1683:ASMTIS>2.0.CO;2](https://doi.org/10.1175/1520-0450(2001)040<1683:ASMTIS>2.0.CO;2), 2001.
- 920
- Dias, J., Tulich, S. N., and Kiladis, G. N.: An Object-Based Approach to Assessing the Organization of Tropical Convection, *J Atmos Sci*, 69, 2488–2504, <https://doi.org/10.1175/JAS-D-11-0293.1>, 2012.
- Elsaesser, G. S., Roca, R., Fiolleau, T., Del Genio, A. D., and Wu, J.: A Simple Model for Tropical Convective Cloud Shield Area Growth and Decay Rates Informed by Geostationary IR, GPM, and Aqua/AIRS Satellite Data, *Journal of Geophysical Research: Atmospheres*, 127, <https://doi.org/10.1029/2021JD035599>, 2022.
- 925
- Endlich, R. M. and Wolf, D. E.: Automatic Cloud Tracking Applied to GOES and METEOSAT Observations, [https://doi.org/10.1175/1520-0450\(1981\)020<0309:ACTATG>2.0.CO;2](https://doi.org/10.1175/1520-0450(1981)020<0309:ACTATG>2.0.CO;2), 1981.
- Esmaili, R. B., Tian, Y., Vila, D. A., and Kim, K. M.: A lagrangian analysis of cold cloud clusters and their life cycles with satellite observations, *J Geophys Res*, 121, 11723–11738, <https://doi.org/10.1002/2016JD025653>, 2016.
- 930
- Evans, J. L. and Shemo, R. E.: A Procedure for Automated Satellite-Based Identification and Climatology Development of Various Classes of Organized Convection, [https://doi.org/10.1175/1520-0450\(1996\)035<0638:APFASB>2.0.CO;2](https://doi.org/10.1175/1520-0450(1996)035<0638:APFASB>2.0.CO;2), 1996.
- Feng, Z., Leung, L. R., Liu, N., Wang, J., Houze, R. A., Li, J., Hardin, J. C., Chen, D., and Guo, J.: A Global High-Resolution Mesoscale Convective System Database Using Satellite-Derived Cloud Tops, Surface Precipitation, and Tracking, *Journal of Geophysical Research: Atmospheres*, 126, <https://doi.org/10.1029/2020JD034202>, 2021.
- 935
- Feng, Z., Hardin, J., Barnes, H. C., Li, J., Leung, L. R., Varble, A., and Zhang, Z.: PyFLEXTRKR: a Flexible Feature Tracking Python Software for Convective Cloud Analysis, 16, 2753–2776, <https://doi.org/10.5194/egusphere-2022-1136>, 2023.
- Fiolleau, T.: Animation of convective situation segmented by TOOCAN from HIMAWARI IR data over the Western Pacific region in October 2015, <https://doi.org/10.5446/68200>, 2024.
- 940
- Fiolleau, T. and Roca, R.: An algorithm for the detection and tracking of tropical mesoscale convective systems using infrared images from geostationary satellite, *IEEE Transactions on Geoscience and Remote Sensing*, 51, <https://doi.org/10.1109/TGRS.2012.2227762>, 2013a.

- 945 Fiolleau, T. and Roca, R.: Composite life cycle of tropical mesoscale convective systems from geostationary and low Earth orbit satellite observations: method and sampling considerations, *Quarterly Journal of the Royal Meteorological Society*, 139, 941–953, <https://doi.org/10.1002/qj.2174>, 2013b.
- Fiolleau, T., Roca, R., Cloche, S., Bouniol, D., and Raberanto, P.: Homogenization of Geostationary Infrared Imager Channels for Cold Cloud Studies Using Megha-Tropiques/ScaRaB, *IEEE Transactions on Geoscience and Remote Sensing*, 58, 6609–6622, <https://doi.org/10.1109/TGRS.2020.2978171>, 2020.
- 950 Guilloateau, C. and Foufoula-Georgiou, E.: Life Cycle of Precipitating Cloud Systems from Synergistic Satellite Observations: Evolution of Macrophysical Properties and Precipitation Statistics from Geostationary Cloud tracking and GPM Active and Passive Microwave Measurements, *J Hydrometeorol*, <https://doi.org/10.1175/jhm-d-23-0185.1>, 2024.
- Harper, B., Kepert, J., and Ginger, J.: Wind speed time averaging conversions for tropical cyclone conditions, in: *Proc. 28th Conference Hurricanes and Tropical Meteorology. (AMS, 2008)*, 2008.
- 955 Heikenfeld, M., Marinescu, P. J., Christensen, M., Watson-Parris, D., Senf, F., Van Den Heever, S. C., and Stier, P.: Tobac 1.2: Towards a flexible framework for tracking and analysis of clouds in diverse datasets, *Geosci Model Dev*, 12, 4551–4570, <https://doi.org/10.5194/gmd-12-4551-2019>, 2019.
- Hennon, C. C., Helms, C. N., Knapp, K. R., and Bowen, A. R.: An objective algorithm for detecting and tracking tropical cloud clusters: Implications for tropical cyclogenesis prediction, *J Atmos Ocean Technol*, 28, 1007–1018, <https://doi.org/10.1175/2010JTECHA1522.1>, 2011.
- 960 Hennon, C. C., Papin, P. P., Zarzar, C. M., Michael, J. R., Adam Caudill, J., Douglas, C. R., Groetsema, W. C., Lacy, J. H., Maye, Z. D., Reid, J. L., Scales, M. A., Talley, M. D., and Helms, C. N.: Tropical cloud cluster climatology, variability, and genesis productivity, *J Clim*, 26, 3046–3066, <https://doi.org/10.1175/JCLI-D-12-00387.1>, 2013.
- 965 Hewison, T. J., Wu, X., Yu, F., Tahara, Y., Hu, X., Kim, D., and Koenig, M.: GSICS inter-calibration of infrared channels of geostationary imagers using metop/IASI, *IEEE Transactions on Geoscience and Remote Sensing*, 51, 1160–1170, <https://doi.org/10.1109/TGRS.2013.2238544>, 2013.
- Hodges, K. I.: A General-Method For Tracking Analysis And Its Application To Meteorological Data, [https://doi.org/10.1175/1520-0493\(1994\)122<2573:AGMFTA>2.0.CO;2](https://doi.org/10.1175/1520-0493(1994)122<2573:AGMFTA>2.0.CO;2), 1994.
- Houze Jr, R. a.: Mesoscale Convective Systems, *Reviews of Geophysics*, 42, 1–43, <https://doi.org/10.1029/2004RG000150>, 2004.
- 970 Houze, R. A.: 100 Years of Research on Mesoscale Convective Systems, *Meteorological Monographs, AMSMONOGRAPHS-D-18-0001.1*, <https://doi.org/10.1175/AMSMONOGRAPHS-D-18-0001.1>, 2018.

- Huang, X., Hu, C., Huang, X., Chu, Y., Tseng, Y. heng, Zhang, G. J., and Lin, Y.: A long-term tropical mesoscale convective systems dataset based on a novel objective automatic tracking algorithm, *Clim Dyn*, 51, 3145–3159, <https://doi.org/10.1007/s00382-018-4071-0>, 2018.
- 975 Jirak, I. L., Cotton, W. R., and Mcanelly, R. L.: Satellite and Radar Survey of Mesoscale Convective System Development, 2428–2449, [https://doi.org/10.1175/1520-0493\(2003\)131<2428:SARSOM>2.0.CO;2](https://doi.org/10.1175/1520-0493(2003)131<2428:SARSOM>2.0.CO;2), 2003.
- Jones, W. K., Christensen, M. W., and Stier, P.: A Semi-Lagrangian Method for Detecting and Tracking Deep Convective Clouds in Geostationary Satellite Observations, <https://doi.org/10.5194/amt-2022-31>, n.d.
- Knapp, K. R., Kruk, M. C., Levinson, D. H., Diamond, H. J., and Neumann, C. J.: The international best track archive for climate stewardship (IBTrACS), *Bull Am Meteorol Soc*, 91, 363–376, <https://doi.org/10.1175/2009BAMS2755.1>, 2010.
- 980 Knapp, K. R., Ansari, S., Bain, C. L., Bourassa, M. A., Dickinson, M. J., Funk, C., Helms, C. N., Hennon, C. C., Holmes, C. D., Huffman, G. J., Kossin, J. P., Lee, H. T., Loew, A., and Magnusdottir, G.: Globally Gridded Satellite observations for climate studies, *Bull Am Meteorol Soc*, 92, 893–907, <https://doi.org/10.1175/2011BAMS3039.1>, 2011.
- Kruk, M. C., Knapp, K. R., and Levinson, D. H.: A technique for combining global tropical cyclone best track data, *J Atmos Ocean Technol*, 27, 680–692, <https://doi.org/10.1175/2009JTECHA1267.1>, 2010.
- 985 Laing, A. G. and Fritsch, J. M.: The Large-Scale Environments of the Global Populations of Mesoscale Convective Complexes, n.d.
- Liu, C., Zipser, E. J., and Nesbitt, S. W.: Global Distribution of Tropical Deep Convection: Different Perspectives from TRMM Infrared and Radar Data, *J Clim*, 20, 489–503, <https://doi.org/10.1175/jcli4023.1>, 2007.
- 990 Liu, C., Zipser, E. J., Cecil, D. J., Nesbitt, S. W., and Sherwood, S.: A cloud and precipitation feature database from nine years of TRMM observations, *J Appl Meteorol Climatol*, 47, 2712–2728, <https://doi.org/10.1175/2008JAMC1890.1>, 2008.
- Machado, L. A. T. and Rossow, W. B.: Structural Characteristics and Radiative Properties of Tropical Cloud Clusters, [https://doi.org/10.1175/1520-0493\(1993\)121<3234:SCARPO>2.0.CO;2](https://doi.org/10.1175/1520-0493(1993)121<3234:SCARPO>2.0.CO;2), 1993.
- Machado, L. A. T., Desbois, M., Duvel, J.-P., Machado, L. A. T., Desbois, M., and Duvel, J.-P.: Structural Characteristics of Deep Convective Systems over Tropical Africa and the Atlantic Ocean, [https://doi.org/10.1175/1520-0493\(1992\)120<0392:SCODCS>2.0.CO;2](https://doi.org/10.1175/1520-0493(1992)120<0392:SCODCS>2.0.CO;2), 1992.
- 995 Machado, L. A. T., Rossow, W. B., Guedes, R. L., and Walker, A. W.: Life Cycle Variations of Mesoscale Convective Systems over the Americas, n.d.
- Maddox, R. A.: Mesoscale Convective Complexes, *Bull Am Meteorol Soc*, 61, 1374–1387, 1980.

- 1000 Mapes, B. and Houze, R. A.: Cloud Clusters and Superclusters over the Oceanic Warm Pool, *Mon Weather Rev*, 121, 1398–1415, [https://doi.org/https://doi.org/10.1175/1520-0493\(1993\)121<1398:CCASOT>2.0.CO;2](https://doi.org/https://doi.org/10.1175/1520-0493(1993)121<1398:CCASOT>2.0.CO;2), 1993.
- Mapes, B., Milliff, R., and Morzel, J.: Composite life cycle of maritime tropical mesoscale convective systems in scatterometer and microwave satellite observations, *J Atmos Sci*, 66, 199–208, <https://doi.org/10.1175/2008JAS2746.1>, 2009.
- Mathon, V. and Laurent, H.: Life cycle of Sahelian mesoscale convective cloud systems, *Quarterly Journal of the Royal*, 1–1005 11, 2001.
- Mohr, K. I. and Zipser, E. J.: Mesoscale Convective Systems Defined by Their 85-GHz Ice Scattering Signature: Size and Intensity Comparison over Tropical Oceans and Continents, *Mon Weather Rev*, 124, 2417–2437, [https://doi.org/10.1175/1520-0493\(1996\)124<2417:mcsdbt>2.0.co;2](https://doi.org/10.1175/1520-0493(1996)124<2417:mcsdbt>2.0.co;2), 1996.
- Ocasio, K. M. N., Evans, J. L., and Young, G. S.: Tracking mesoscale convective systems that are potential candidates for tropical cyclogenesis, *Mon Weather Rev*, 148, 655–669, <https://doi.org/10.1175/MWR-D-19-0070.1>, 2020.
- 1010 Poujol, B., Prein, A. F., and Newman, A. J.: Kilometer-scale modeling projects a tripling of Alaskan convective storms in future climate, *Clim Dyn*, 55, 3543–3564, <https://doi.org/10.1007/s00382-020-05466-1>, 2020.
- Prein, A. F., Feng, Z., Fiolleau, T., Moon, Z. L., Núñez Ocasio, K. M., Kukulies, J., Roca, R., Varble, A. C., Rehbein, A., Liu, C., Ikeda, K., Mu, Y., and Rasmussen, R. M.: Km-Scale Simulations of Mesoscale Convective Systems Over South America—1015 A Feature Tracker Intercomparison, *Journal of Geophysical Research: Atmospheres*, 129, <https://doi.org/10.1029/2023JD040254>, 2024.
- Rajagopal, M., Russell, J., Skok, G., and Zipser, E.: Tracking Mesoscale Convective Systems in IMERG and Regional Variability of Their Properties in the Tropics, *Journal of Geophysical Research: Atmospheres*, 128, <https://doi.org/10.1029/2023JD038563>, 2023.
- 1020 Roca, R. and Fiolleau, T.: Extreme precipitation in the tropics is closely associated with long-lived convective systems, *Commun Earth Environ*, 1, <https://doi.org/10.1038/s43247-020-00015-4>, 2020.
- Roca, R. and Ramanathan, V.: Scale dependence of monsoonal convective systems over the Indian Ocean, *J Clim*, 13, 1286–1298, [https://doi.org/10.1175/1520-0442\(2000\)013<1286:SDOMCS>2.0.CO;2](https://doi.org/10.1175/1520-0442(2000)013<1286:SDOMCS>2.0.CO;2), 2000.
- Roca, R., Berges, J. C., Brogniez, H., Capderou, M., Chambon, P., Chomette, O., Cloche, S., Fiolleau, T., Jobard, I., and 1025 Lemond, J.: On the water and energy cycles in the Tropics, *Comptes Rendus Geosciences*, 342, 390–402, <https://doi.org/doi.org/10.1016/j.crte.2010.01.003>, 2010.
- Roca, R., Aublanc, J., Chambon, P., Fiolleau, T., and Viltard, N.: Robust observational quantification of the contribution of mesoscale convective systems to rainfall in the tropics, *J Clim*, 27, <https://doi.org/10.1175/JCLI-D-13-00628.1>, 2014.

- 1030 Roca, R., Fiolleau, T., and Bouniol, D.: A simple model of the life cycle of mesoscale convective systems cloud shield in the tropics, *J Clim*, 30, <https://doi.org/10.1175/JCLI-D-16-0556.1>, 2017.
- Roca Rémy, Bouniol, D., and Fiolleau Thomas: On the Duration and Life Cycle of Precipitation Systems in the Tropics, in: *Satellite Precipitation Measurement: Volume 2*, edited by: Levizzani Vincenzo and Kidd, C. and K. D. B. and K. C. D. and N. K. and T. F. J., Springer International Publishing, Cham, 729–744, [https://doi.org/10.1007/978-3-030-35798-6\\_14](https://doi.org/10.1007/978-3-030-35798-6_14), 2020.
- 1035 Schröder, M., König, M., and Schmetz, J.: Deep convection observed by the Spinning Enhanced Visible and Infrared Imager on board Meteosat 8: Spatial distribution and temporal evolution over Africa in summer and winter 2006, *Journal of Geophysical Research Atmospheres*, 114, 1–14, <https://doi.org/10.1029/2008JD010653>, 2009.
- Sven Ostlund, S.: NOAA Technical Memorandum ERL WMP0-15 Computer Software for Rainfall Analyses and Echo Tracking of Digitized Radar Data, 1974.
- 1040 Szantai, A., Six, B., Cloché, S., and Sèze, G.: megha-tropiques MTTM Megha-Tropiques Technical Memorandum Quality of geostationary satellite images Megha-Tropiques Quality of geostationary satellite images, 2011.
- Tan, J., Jakob, C., Rossow, W. B., and Tselioudis, G.: Increases in tropical rainfall driven by changes in frequency of organized deep convection, *Nature*, 519, 451–454, <https://doi.org/10.1038/nature14339>, 2015.
- Tsakraklides, G. and Evans, J. L.: Global and regional diurnal variations of organized convection, *J Clim*, 16, 1562–1572, <https://doi.org/10.1175/1520-0442-16.10.1562>, 2003.
- 1045 Vant-Hull, B., Rossow, W., and Pearl, C.: American Meteorological Society Global Comparisons of Regional Life Cycle Properties and Motion of Multiday Convective Systems: Tropical and Midlatitude Land and Ocean, *Source: Journal of Climate*, 29, 5837–5858, <https://doi.org/10.2307/26385605>, 2016.
- Wilcox, E. M.: Spatial and temporal scales of precipitating tropical cloud systems in satellite imagery and the NCAR CCM3, *J Clim*, 16, 3545–3559, [https://doi.org/10.1175/1520-0442\(2003\)016<3545:SATSOP>2.0.CO;2](https://doi.org/10.1175/1520-0442(2003)016<3545:SATSOP>2.0.CO;2), 2003.
- 1050 Williams, M. and Houze, R. A.: Satellite-Observed Characteristics of Winter Monsoon Cloud Clusters, [https://doi.org/10.1175/1520-0493\(1987\)115<0505:SOCOWM>2.0.CO;2](https://doi.org/10.1175/1520-0493(1987)115<0505:SOCOWM>2.0.CO;2), 1987.
- Woodley, W. L., Cecilia G. Griffith, Joseph S. Griffin, and Scott C. Stromatt.: The Inference of GATE Convective Rainfall from SMS–1 Imagery., *Journal of Applied Meteorology* , 19, 388–408, 1980.